OXFORD

Journal of Petrology, 2024, **65**, egae017
https://doi.org/10.1093/petrology/egae017
Advance access publication date 29 February 2024
Original Manuscript

Olivine-Hosted Melt Inclusions Track Progressive Dehydration Reactions in Subducting Slabs Across Volcanic Arcs

Raimundo Brahm [1,*], Daniel Coulthard Jr [2,†], Georg Zellmer [2], Takeshi Kuritani [3], Naoya Sakamoto [4], Hajime Taniuchi [5,6], Hisayoshi Yurimoto [4], Mitsuhiro Nakagawa [3] and Eiichi Sato [7]

[1]School of Geography, Environment and Earth Sciences, Te Herenga Waka—Victoria University of Wellington, PO Box 600, Wellington 6140, New Zealand
[2]School of Agriculture and Environment, Massey University, Private Bag 11 222, Palmerston North 4442, New Zealand
[3]Graduate School of Science, Hokkaido University, 8 Kita 10 Jonishi, Kita Ward, Sapporo, Hokkaido 060-0810, Japan
[4]Isotope Imaging Laboratory , Creative Research Institution, Hokkaido University, Sapporo, Hokkaido 001-0020, Japan
[5]Department of Geoscience, Faculty of Science, Shizuoka University, Shizuoka 422-8529, Japan
[6]Geological Survey of Japan, National Institute of Advanced Industrial Science and Technology, Tsukuba 305-8567, Japan
[7]Earth Science Laboratory, Hokkaido University of Education, Asahikawa, Hokkaido 070-0825, Japan

*Corresponding author. Telephone: (+64) 2102270893. E-mail: raimundo.brahmscott@vuw.ac.nz
†Present address: School of Geography, Environment and Earth Sciences, Cotton Building, Victoria University of Wellington, Kelburn, Wellington 6140, New Zealand

The stability and breakdown of mineral phases in subducting slabs control the cycling of trace elements through subduction zones. Stability of key minerals and the partitioning of trace elements between these minerals and liquid phases of interests have been charted by natural sample analysis and experimental constraints. However, systematic study from arc front to far back arc has rarely shown that the expected geochemical variations of the slab liquid are actually recorded by natural samples. Complexities arise by uncertainties on the nature of the slab component (melts, fluids and supercritical liquids), source heterogeneities and transport processes. Using data from olivine-hosted melt inclusions sampled along and across the NE Japan and southern Kurile arcs, we demonstrate that experimentally and thermodynamically constrained phase stabilities in subducted materials indeed control the trace element signatures as predicted by these models and experiments. The main reactions that can be traced across arc are progressive breakdown of light rare earth element-rich accessory phases (e.g. allanite), enhanced dehydration of the lithospheric mantle (serpentine breakdown) and changes in the nature of the slab component. This work elucidates subduction zone elemental cycling in a well-characterized petrogenetic setting and provides important constraints on the interpretation of trace element ratios in arc magmas in terms of the prograde metamorphic reactions within the subducting slab.

Key words: NE Japan arc; Kuril arc; Island arc magmatism; subduction element cycling; prograde metamorphic reactions

INTRODUCTION

There is consensus on the participation of a slab component in the generation of magmatism in subduction zones (Gill, 1981; Tatsumi *et al.*, 1986; Grove *et al.*, 2006). This slab material is responsible for the enrichment in some trace and volatile elements of arc magmas compared to mid-ocean ridge basalts (Perfit *et al.*, 1980; Pearce, 1983). Nonetheless, there is continuing debate regarding the nature of the slab component and the processes that govern its composition. Slab liquids have been interpreted as hydrous fluids generated by dehydration reactions during prograde metamorphism (e.g. Plank & Langmuir, 1998; Schmidt & Poli, 1998; Hacker, 2008), H_2O-rich silicate melts produced by partial melting of the altered oceanic crust (AOC) and/or its sedimentary cover (SED) (e.g. Manning, 2004; Kimura *et al.*, 2010) and supercritical fluids (*e.g.* Kessel *et al.*, 2005; Taniuchi *et al.*, 2020).

Additional complexities arise from the variable involvement of different sources within the subducted slab on the resulting slab component. The proportions of the AOC and SED components have usually been estimated using radiogenic isotopic data (e.g. Moriguti *et al.*, 2004; Kuritani *et al.*, 2019; Kuritani *et al.*, 2021). Further involvement of fluids percolating through the slab, originating from serpentine breakdown within the hydrated subducted lithospheric mantle, has also been proposed as an important fluid source (Straub & Layne, 2003; Barnes *et al.*, 2008; Kendrick *et al.*, 2014; Kendrick *et al.*, 2020). Another possible source of fluid is the dehydration of the mantle wedge, hydrated during pore fluid release of the slab in the forearc and dragged downwards by the subducting slab (Tatsumi, 1986; Tatsumi *et al.*, 1986; Tatsumi, 1989).

Different mechanisms of transport for the slab component through the mantle wedge have been proposed. Melting is triggered when the solidus is depressed as slab fluids ascent through the mantle wedge with an inverted geotherm from the slab surface to the hot core of the mantle wedge. This

Received: November 2, 2022. **Revised:** January 23, 2024. **Accepted:** February 18, 2024

inverted geotherm is generated by the cooling of the mantle wedge from the subducted slab and the corner flow that occurs due to viscous coupling of the mantle wedge with the slab (Tovish *et al.*, 1978). Less viscous hydrous slab liquids may ascend vertically through percolation, generating an initial H_2O-rich melt when reaching the solidus temperature and reacting continuously with the mantle as the temperature increases and pressure decreases upward. Progressive mantle melting reduces the H_2O content of the melt (Gaetani *et al.*, 2003; Grove *et al.*, 2006). If the overlying mantle wedge is not previously saturated in volatiles at forearc depths, the slab liquids will react with the mantle to form hydrated minerals (chlorite, serpentine, phlogopite) that are dragged down by mantle flow and will release fluids further down, when breakdown temperatures/pressures of these hydrous phases are reached and accumulated mantle melts above the solidus temperature can ascend diapirically, producing a component of adiabatic melting (Tatsumi, 1986; Tatsumi *et al.*, 1986; Tatsumi, 1989). Slab material can also be transported as buoyant diapirs, which might be pushed further away from the trench by the downward corner flow, and can consist of viscous slab melts or as geochemical and mechanical mixtures of mantle–AOC–SED component (melange) (Marschall & Schumacher, 2012; Nielsen & Marschall, 2017; Cruz-Uribe *et al.*, 2018; Corella Santa Cruz *et al.*, 2023; D'Mello *et al.*, 2023).

There is also some debate on the control and behaviour of trace elements during extraction of liquids from the slab. The partitioning behaviour of trace elements between SED, AOC and mantle lithologies with melts or fluids have been studied through analysis of exhumed high-grade metamorphic complexes (e.g. Sorensen *et al.*, 1997; Hermann, 2002; John *et al.*, 2011; Martin *et al.*, 2014; Pagé & Hattori, 2017) and dehydration/melting experiments (e.g. Schmidt & Poli, 1998; Hermann & Green, 2001; Hermann, 2002; Kessel *et al.*, 2005; Spandler *et al.*, 2007; Hermann & Spandler, 2008; Hermann & Rubatto, 2009; Dalou *et al.*, 2012; Krenn *et al.*, 2012; Li & Hermann, 2017; Tsay *et al.*, 2017). Kessel *et al.* (2005) conducted high-pressure–temperature (PT) experiments on a basaltic eclogite sample, recovering partitioning data describing equilibrium between fluids (700–900°C at 4 GPa), melt (1000°C at 4 GPa) and supercritical fluids (800–1200°C at 6 GPa) and major residual mineral components (garnet and clinopyroxene) and accessory rutile, which retains Nb, Ta and Ti (Foley *et al.*, 2000). Analysis of natural samples and experiments of sediment and basalt melting (Hermann, 2002; Spandler *et al.*, 2007; Hermann & Rubatto, 2009; Tsay *et al.*, 2017) have shown the importance of accessory phases in controlling the trace element concentrations in the fluid/melt. Allanite and monazite have been shown to carry most of the light rare earth elements (LREEs) and Th in eclogitic metasediments and metabasites, whereas phengite controls the large ion lithophile element (LILE) budget, and zircon carries most of the Zr. Saturation of these phases with increasing T controls the slab melt composition. During dehydration, the presence of these accessory phases reduces the capability of the fluid to transport all REE, thereby masking the systematic increase in mobility from heavy REE (HREE) to LREE expected from the presence of a garnet residue.

Various studies have analysed across-arc variations in geochemical signatures (e.g. Stolper & Newman, 1994; Patino *et al.*, 1997; Moriguti *et al.*, 2004; Kelley *et al.*, 2006; Portnyagin *et al.*, 2007; Kelley *et al.*, 2010; Tollstrup *et al.*, 2010; Jacques *et al.*, 2013; Jacques *et al.*, 2014; Kimura & Nakajima, 2014), but the rarely found correlations between predicted prograde metamorphic reactions in the slab and across-arc variations in slab component signatures have usually been tied to all the complexities in the nature of the slab component, variable source compositions and transport mechanisms.

The NE Japan and southern Kurile arcs comprise a well constrained subduction setting with a broad distribution of volcanoes with respect to their distance from the trench. It therefore presents an opportunity to relate geochemical variations to changes in slab PT conditions. This study presents the trace and volatile element contents of well-characterized olivine-hosted melt inclusions (MIs) from tephra samples of seven volcanoes along and across the northernmost NE Japan arc and southernmost Kurile arc. The systematics of how trace and volatile element ratios vary with estimated slab surface temperature (T_{slab}) conditions are investigated to study the across-arc transitions in the composition and nature of the slab component. We show that variations from arc to back arc geochemical signatures track the progressive breakdown of accessory phases, progressive involvement of the lithospheric mantle fluids and changes in the nature of the slab component.

TECTONIC SETTING

The Tohoku and Hokkaido regions comprise the northernmost section of the NE Japan arc and the southernmost section of the Kuril arc (Fig. 1), both formed by the westward subduction of the Pacific plate beneath the Okhotsk Plate (7–11 cm/yr; Bird, 2003; Northrup *et al.*, 1995) at the eastern margin of northern Japan. Both arcs meet in central Hokkaido, where the strike of the trench shifts from N56E in the Kuril arc to N10E in the NE Japan arc. The two arcs meet in the Hidaka collision zone, caused by the southward migration of the Kuril fore arc sliver (Kimura, 1996; Kita *et al.*, 2014), which has been colliding with the NE Japan fore arc since the Miocene (*c.* 12 Ma), uplifting the Hidaka Mountains. This collision zone coincides with the position of the southernmost volcano of the Kuril arc (Tokachidake). There is a *c.* 120 km long volcanic gap between Tokachidake and the northernmost active volcano of the NE Japan arc in central Hokkaido.

For the last *c.* 5 Ma, the location of the arc front in NE Honshu and Hokkaido has remained in the same place (Martin, 2011; Yoshida *et al.*, 2014). The first *c.* 3 Myr of this period is characterized by caldera-dominated felsic activity. At *c.* 2 Ma, the activity changed to stratovolcano-dominated basaltic to andesitic volcanism (Acocella *et al.*, 2008), which was associated with a shift in compression orientation from NE–SW to the current ENE–WSW orientation.

The samples analysed in this study belong to seven volcanic systems distributed along and across the northernmost NE Japan arc and the southernmost Kuril arc. In the NE Japan arc, Akita-Komagatake (AK) and Hakkoda (HK) volcanoes at the arc front and Oshima–Oshima (OO) volcano in the back arc were sampled. In the Kuril arc, Tokachidake (TK), Akan-fuji (AKN) and Tya–Tya (TT) volcanoes at the arc front and Rishiri (RSH) volcano in the back arc were sampled. A brief description of each arc front volcanic unit can be found in Brahm *et al.* (2022). Here, we provide a brief description of the back-arc volcanic systems.

Oshima–Oshima

The OO volcanic system corresponds to a volcanic island in the back arc of the northernmost section of the NE Japan arc, off the SW coast of Hokkaido. The general geology of OO is described by Katsui & Satoh, (1970). It consists in three overlayed volcanic edifices: Higashi-yama, Nishi-yama and the central cone. Higashi-yama somma is located in the eastern section of the island and is

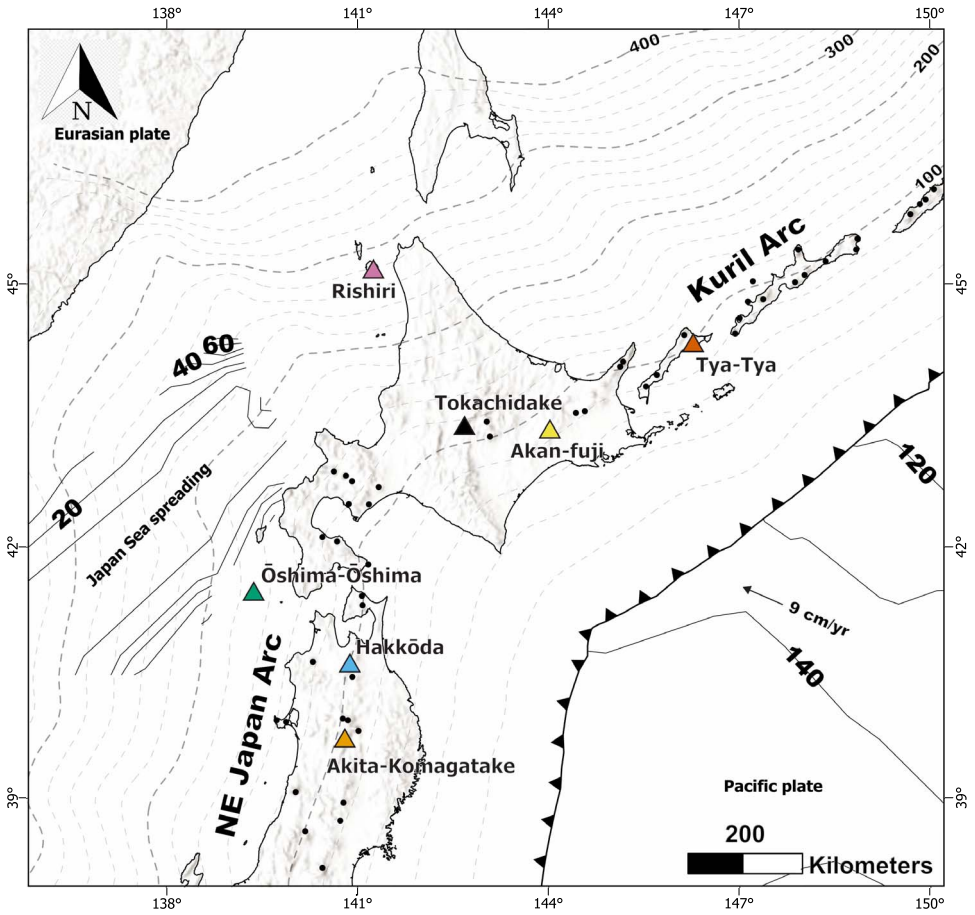

Fig. 1. Map of NE Japan. Triangles are the volcanoes studied here. Black dots are other volcanoes. The black line with triangles marks the trench. Grey dashed lines indicate the depth of the slab (in km). The thin black lines with bold numbers indicate the age of the seafloor (in Ma).

the oldest edifice. It surrounds a caldera, and it is thought to have been formed in the late Pleistocene. Its eruptive history consists of early andesites followed by basalts. The main edifice and the caldera were formed by the basaltic activity. This activity was followed by a period of quiescence and erosion. The formation of Nishi-yama started with basaltic and andesitic activity from the western part of the caldera, follow by subsidence of this new edifice to form a second caldera (760 ± 70 years; Katsui & Satoh, 1970) after the eruption of andesitic pumice and basaltic scoria. The central cone was formed by the eruption of basalts from the caldera in Nishi-yama somma during historic activity that started with the 1741–1742 eruption. Basaltic lava flows were extruded from flank eruptions, which flowed into the sea at the northern coast. Known historic activity ranges from 1741 to 1790, including ash fall and gas emission events. Most rocks are alkali rich with high K_2O/Na_2O and MgO/FeO_T ratios. Basalts tend to be silica undersaturated, whereas andesites are silica-oversaturated and follow a calc-alkaline trend. The selected sample belongs to the basaltic tephra fall deposit from the 1741 to 1742 eruption.

Rishiri

The RSH island is a volcanic island in the back arc of the southernmost Kuril arc, offshore to the west of NW Hokkaido. A detailed description of the stratovolcano evolution is given by (Kobayashi, 1987) and (Ishizuka & Nakagawa, 1999) The evolution of RSH is divided into three main stages. In the Early stage, activity was dominated by andesitic lavas, pyroclastic flows and dacitic lava dome formation. The main stratovolcano was built during the middle stage with lava and pyroclastic flows, where calc-alkaline andesite was the predominant composition. The Late stage was dominated by the production of alkali lavas, trachytic andesites and minor dacitic and rhyolitic pumice. During the late stage, a series of scoria cones with lava flows developed in the SE flank of the main cone (Kuritani *et al.*, 2008), which erupted at *c.* ≤ 20 ka (Kuritani *et al.*, 2007). The sample analysed in this study was taken from the southern flank of the Senpoushi scoria cone.

SAMPLES AND METHODS

The MIs from arc front tephra samples in this study were previously analysed for major elements in Brahm *et al.* (2022). The present study includes a new set of major element analyses of 40 MIs and their olivine hosts from the back-arc tephra samples, which were analysed with a JXA-8230 SuperProbe electron probe micro-analyzer (EPMA) at Victoria University, New Zealand.

In addition, volatile components (H_2O, CO_2, S, Cl and F) were analysed with the Cameca ims-1270 secondary ion mass spectrometer (SIMS) at Hokkaido University. A subset of 33 MIs was analysed for trace elements with a RESOlution-SE Compact 193 nm excimer laser ablation system in tandem with an Agilent 8900 Inductively Coupled Plasma – Mass Spectrometer (LA ICP-MS) at Waikato University in Hamilton, New Zealand. Whole rock trace element analysis was conducted in all samples with the same laser ablation instrument in the glass beads used for major elements analysis. See Supplementary Material for details

of analytical procedures, conditions and uncertainties for halogen and trace element analyses.

X-ray Fluorescence (XRF)

Glass beads were prepared from whole rock powders of the tephra samples. To prepare the glass beads, each sample was first cleaned in an ultrasonic bath with distilled water. Samples were then dried in an oven at 100°C for at least 2 hours or overnight at 45°C. Samples were then powdered in a tungsten carbide mill and kept in the oven at 100°C for at least 2 hours. Loss of ignition was determined by weighting *c.* 2 g of powder before and after heating in an oven at *c.* 900°C for 3 hours. After ignition, *c.* 0.8 g of the powdered sample was mixed with *c.* 8.0 g of a flux of a lithium metaborate:lithium tetraborate mixture (12: 22), followed by fusion to produce a glass disc using a XRFuse2 electric fusion apparatus.

Major element concentrations were measured with a 1 kW Bruker Tiger S8 Series II XRF spectrometer at Massey University in Palmerston North, New Zealand. Interference-corrected spectra intensities were converted to oxide concentrations using calibration curves consisting of natural standards closely approximating the mafic matrix of our samples. The long-term reproducibility of Oreas 24c standard reference material was better than ±1% relative (1σ) for all elements except MnO, for which it was better than ±1.5% relative.

EPMA

Plagioclase crystals were analysed using a defocused beam of a 10 μm diameter with an acceleration potential of 15 kV and an electron beam current of 12 nA. Pyroxene crystals were analysed using a focused beam with an acceleration potential of 20 keV and an electron beam current of 30 nA. Counting times were 40 s on peak and 15 s on background for all elements in both mineral phases. Na was analysed first to avoid Na migration.

For olivine crystals, analysis spots were chosen in the vicinity of the MIs to better constrain equilibrium conditions. A focused beam with acceleration potential of 20 keV was used with an electron beam current of 30 nA for Si, Fe, Mg, Mn and Ti, and 100 nA for Al, Ni, Ca and Cr. Counting times were 40 s on peak and 15 s on background for all elements but Ca, with 400 s on peak and 20 s on background. Accuracy and reproducibility of the analyses was constrained by alternated analysis of USNM2566 and JK3 olivine secondary standards during the session. Concentrations are accurate to <4% for major elements, < 35% for Mn, < 24% for Ni and < 89% for Cr. Accuracy of Ca was <7%. Ti and Al were usually below the detection limits for both standards. Reproducibility estimates (as 1σ) were < 2% for major elements, *c.* 3% for Ni and Ca, *c.* 5% for Mn and *c.* 27% for Cr.

Analysis of MI compositions (Si, Ti, Al, Fe, Mn, Mg, Ca, Na, K, and P or Cr) were performed with an accelerating potential of 15 keV and an electron beam current of 8 nA. A defocused beam of 5–10 μm diameter was used and Na was analysed first to avoid Na migration. Basaltic glass secondary standards (VGA99 and BHVO-2G) were analysed periodically throughout the session to test for instrumental drift and to constrain accuracy and reproducibility of the analyses. Reproducibility estimates (1σ) are <1% for SiO_2, Al_2O_3 and CaO, *c.* 2% for FeO and MgO, *c.* 3% for Na_2O and K_2O, *c.* 10% for TiO_2, MnO and P_2O_5. Accuracies are <1% for most SiO_2 and Al_2O_3 secondary standard analyses, < 2% for most Al_2O_3, FeO, MgO and CaO analyses, < 3% for most K_2O analyses, < 10% for most Na_2O and TiO_2 analyses and < 20% for most P_2O_5 analyses.

The S composition for all reference glasses for volatile measurements (see below) was measured by repeated high precision analysis with the EPMA. Ten S measurements of each reference glass were performed, where the average result was used as the reference value with the associated standard deviation as the propagated error used for SIMS calibration. Analysis conditions consisted of an acceleration voltage of 15 kV, an electron current beam of 8 nA with a 10 μm diameter defocused beam. Primary standard for calibration of S concentration in the reference glasses was the Elba Pyrite. Precision uncertainties (1σ) were < 4%, except for the volatile poor glasses (<15 μg/g for BIR-1G and BHVO-2G). Accuracy was tested using VG99 and VG2 as secondary standards, showing a relative error of <10% for most analyses.

SIMS

Exposed MIs were pressed down into an indium plug mounted in an aluminium disk to avoid H and C contamination from epoxy. The plug was then coated with gold and loaded into the SIMS sample chamber to remain under vacuum for 3 days before analysis to reduce H contamination.

A Cs^+ ion primary beam was used to analyse for ^{1}H, ^{12}C, ^{19}F, ^{30}Si, ^{32}S and ^{35}Cl isotopes. Pre-sputtering of a 25 × 25 μm area was conducted before each analysis with a beam current of 1 nA for 100 s, plus a beam centring time of 96 s. Analysis was carried out with a beam current of 0.1 nA in a 3–5 μm wide area of Gaussian shape. Field aperture was set to 2000 μm with an entrance slit of 60 μm, an energy slit of 25 μm, a contrast aperture of 100 μm and an exit slit of 400 μm. Mass resolution was set to 3243 to avoid interference of isotopic signals (mainly $^{34}S^{1}H$ on ^{35}Cl, $^{29}Si^{1}H$ on ^{30}Si, and $^{31}P^{1}H$ on ^{32}S). The isotopes were measured in five consecutive cycles of 10 s of waiting time and 3 s of analysis time for ^{1}H, 4 s waiting time and 5 s analysis time for ^{12}C and 2 s waiting time and 1 s analysis time for the remaining isotopes (^{19}F, ^{30}Si, ^{32}S and ^{35}Cl). Including pre-sputtering time, each analysis lasted *c.* 8 min. The reproducibility of counts ratios between each volatile and matrix was obtained from the five cycles per analysis. Maximum uncertainties of reproducibility are <10% for $^{1}H/^{30}Si$, <13% for $^{12}C/^{30}Si$ and < 3% for $^{19}F/^{30}Si$, $^{32}S/^{30}Si$ and $^{35}Cl/^{30}Si$.

Reference glasses were polished and mounted in the same indium plug with the MIs and were repeatedly measured during the same analysis session to produce the calibration lines and check for instrument drift. The reference glasses used were BIR-1G and BHVO-2G synthetic standard glasses (USGS), plus CL DR-1, Gal 1652, LS 427, 2πD43, SAM 76–11, SAM 73–12 and SAM 74–2 natural volcanic glasses (Kendrick *et al.*, 2017). F and Cl values for the synthetic glasses were obtained from Marks *et al.* (2017) and Kendrick *et al.* (2018), whereas values for natural samples were taken as the revised compositions of Kendrick *et al.* (2017). H_2O and CO_2 compositions for most of the reference materials were measured using a micro-FTIR instrument (see Brahm *et al.*, 2022 and Supplementary Material) and S was remeasured by EPMA (see above).

Calibration of the SIMS analyses was produced using a maximum likelihood linear regression scheme considering the uncertainties related to SIMS analysis precision and uncertainties in the reference values used. After calibration, the uncertainties in accuracy (1σ) for the volatile species in MIs are *c.* 4% for H_2O, <15% for CO_2 (for concentrations above 50 μg/g), <8% for most S analyses, *c.* 2% for Cl and < 8% for most F analyses.

LA ICP-MS

After XRF analysis, the glass beads were piled up and glued together with epoxy then a slice of the stack was cut, polished and mounted in a glass slide. The analysis was conducted by

pulsing the laser at 10 Hz with a 100 μm spot size and energy density of 5.0 j/cm^2 with an ablation time of 45 s. Ultra-high purity helium was used as the carrier gas (370 mL/min) to deliver the ablated sample for the LA system to the ICP-MS. The ICP-MS was optimized to maximum sensitivity daily (see Supplementary Material for operation conditions). Background counts (gas background, measured with the laser off) were collected for 30 s between samples. NIST610 and NIST612 glass standards were analysed after every 10 samples to account for any instrument drift. Analysis conditions for MI glasses are the same as for the glass beads, except that the laser size spot was varied between 50 and 100 μm depending on the MI size. Standard glasses were measured with each laser spot size used to be able to obtain the concentrations of trace element in the MIs analysed at each different spot size.

Data processing was performed using Iolite (v3.32, Patton *et al.*, 2011). Background counts were subtracted from the raw data and all data were standardized to the NIST612 glass. NIST610 glass was used as a secondary standard. The GeoReM database (Jochum *et al.*, 2005) was utilized for the standard glass values. The whole rock real concentrations were calculated by mass balance calculations using the LA ICP-MS results and the proportion of sample and flux measured when producing the glass beads.

RESULTS

Petrography and mineral chemistry

A detailed petrographic description of arc front samples was published in Brahm *et al.* (2022). A summary is shown here, followed by a more detailed description of back-arc samples.

Arc front

All arc front tephra samples are composed of groundmass (*c.* 50 to 85 vol%) and different proportions phenocrysts. Groundmass is glass rich in all samples except for AKN, where the tephra contains two different types of fragments, one with a crystalline groundmass and another with glass-rich groundmass.

The phenocrysts are mainly olivine (Ol), plagioclase (Pl), clino- and orthopyroxene (Cpx and Opx). Titano-magnetite (Ti-Mag) is present in two of the samples (TK and AKN). Crystal clots are abundant in all samples. The most abundant phenocryst phase is Pl, with >75 vol% of the crystal cargo. These crystals are generally complexly zoned, with An-rich core and a An-poor oscillatory rim. Resorption and sieve textures are common in many Pl populations. The most common pyroxene phase is Cpx, with Opx appearing generally as reaction rims and coronas in Ol and Cpx phenocrysts. Opx phenocrysts are common only in the HK sample.

Ol phenocrysts are scarce in most samples, with <7 vol% of crystal cargo in all but one sample (TT has *c.* 12 vol% Ol). Two different populations of Ol are observed in AK, HK, TK and AKN, and MIs were found exclusively in one of the Ol populations of AK and TK.

Oshima–Oshima

The OO tephra is constituted of a glass-rich groundmass (*c.* 65 vol% in a vesicle free basis) with microlites of Ol and plagioclase Pl (Fig. 2a, c and e). The crystal cargo is composed of *c.* 47 vol% Pl, *c.* 32 vol% Ol, *c.* 20 vol% Cpx and < 1 vol% chrome-spinel (Cr-Sp). The Pl crystals range in size from <0.1 mm to *c.* 2.5 mm.

Most Pl crystals have a wide Ca-rich core of $An_{83–92}$ (Fig. 3a), followed by a narrow rim of $An_{68–78}$. These Pl crystals are found as isolated crystals or as part of Ol + Cpx + Px(+Cr-Sp) clots. The biggest Pl crystals contain a mantled zone of $An_{72–85}$, and sometimes a core with complex oscillatory zoning. Some of these cores include a Ca-rich inner core surrounded by very Ca-poor oscillatory zoning ($An_{42–52}$). In general, the Pl crystals are euhedral to subhedral.

The Ol crystals range between <0.1 mm to 2.4 mm in size and are euhedral to subhedral, with scarce evidence of resorption in some crystals. The most abundant Ol consists of normally zoned crystals with high-Fo cores ($Fo_{81–89}$) (Fig. 3c). The other Ol type consists of Fo-poorer cores ($Fo_{74–79}$) with inverse zoning. Compositions of Ol rims reach Fo_{67}, but most rim compositions do not reach lower Mg contents than Fo_{75}. One crystal was observed with an Opx corona. Both Ol types can be found associated with Cpx in clots, with Cr-Sp inclusions and containing glassy MIs.

The Cpx crystals (< 0.1 mm to *c.* 1 mm wide) are mostly diopside to high-Ca augite (Fig. 3b). The crystal shapes vary from euhedral to anhedral, with mild concentric oscillatory zoning or sector zoning. Some crystals show a high-Ca core with resorption features followed by regular oscillatory zoning. Crystals are found isolated or forming clots with the other mineral phases.

Phenocrysts of Cr-Sp are scarce, but Cr-Sp inclusions are very common in Ol, and Cr-poor spinel inclusions are found in Cpx crystals. Most Cr-Sp inclusions are Fe-poor, with similar cation proportions of Cr and Al (see the Supplementary Material).

Rishiri (RSH)

The RSH tephra is constituted of *c.* 81 vol% groundmass and *c.* 19 vol% crystals (Fig. 2b, d and f). The groundmass is crystal-rich with Pl, Ol and Fe–Ti oxide crystals. The phenocryst cargo is composed of *c.* 64 vol% Pl, *c.* 34 vol% Ol and *c.* 2 vol% Cr-Sp. The Ol crystals are euhedral to subhedral and commonly found as isolated crystals or associated with smaller Pl crystals and Cr-Sp inclusions (Fig. 2d). Core composition range from Fo_{79} to Fo_{85} and are normally zoned, with the rim compositions reaching Fo_{76}.

The Pl crystals of the RSH sample are smaller than the Ol crystals and are euhedral with elongated tabular texture (high aspect ratio). Most Pl crystals are normally zoned with a core of $An_{68–78}$ and rims of $An_{54–69}$. Some Pl crystals include a resorbed core with an overgrown rim of high An composition. Cr-Sp are abundant as inclusions in Ol crystals, some reaching up to *c.* 100 μm in size. These crystals have a higher Al and lower Cr content than the Cr-Sp inclusion in the OO sample (see Supplementary Material).

MI chemistry

Most MIs are glassy (no daughter minerals) and have shrinkage bubbles (Fig. 4). Formation of daughter minerals scarce in MIs from TK (Brahm *et al.*, 2022). Here, we show the major, volatile and trace element contents of the MI glasses.

Major elements

Measured compositions of MI glasses (Fig. 5) show a trend of increasing alkalinity from the NE Japan arc (AK and HK) to the Kuril arc (AKN and TT), followed by TK, RSH and OO with the highest K_2O concentrations. The AK and HK samples are low-K tholeiites, whereas AKN, TT, TK and RSH follow a calc-alkaline trend (Peccerillo & Taylor, 1976). The OO samples have compositions ranging from calc-alkaline to alkaline with most compositions in the high-K calc-alkaline series.

Trace elements

The spider diagrams normalized to primitive mantle for all seven volcanoes (Fig. 6a, c and e) show the characteristic patterns of arc volcanism related to contamination of the source by a slab

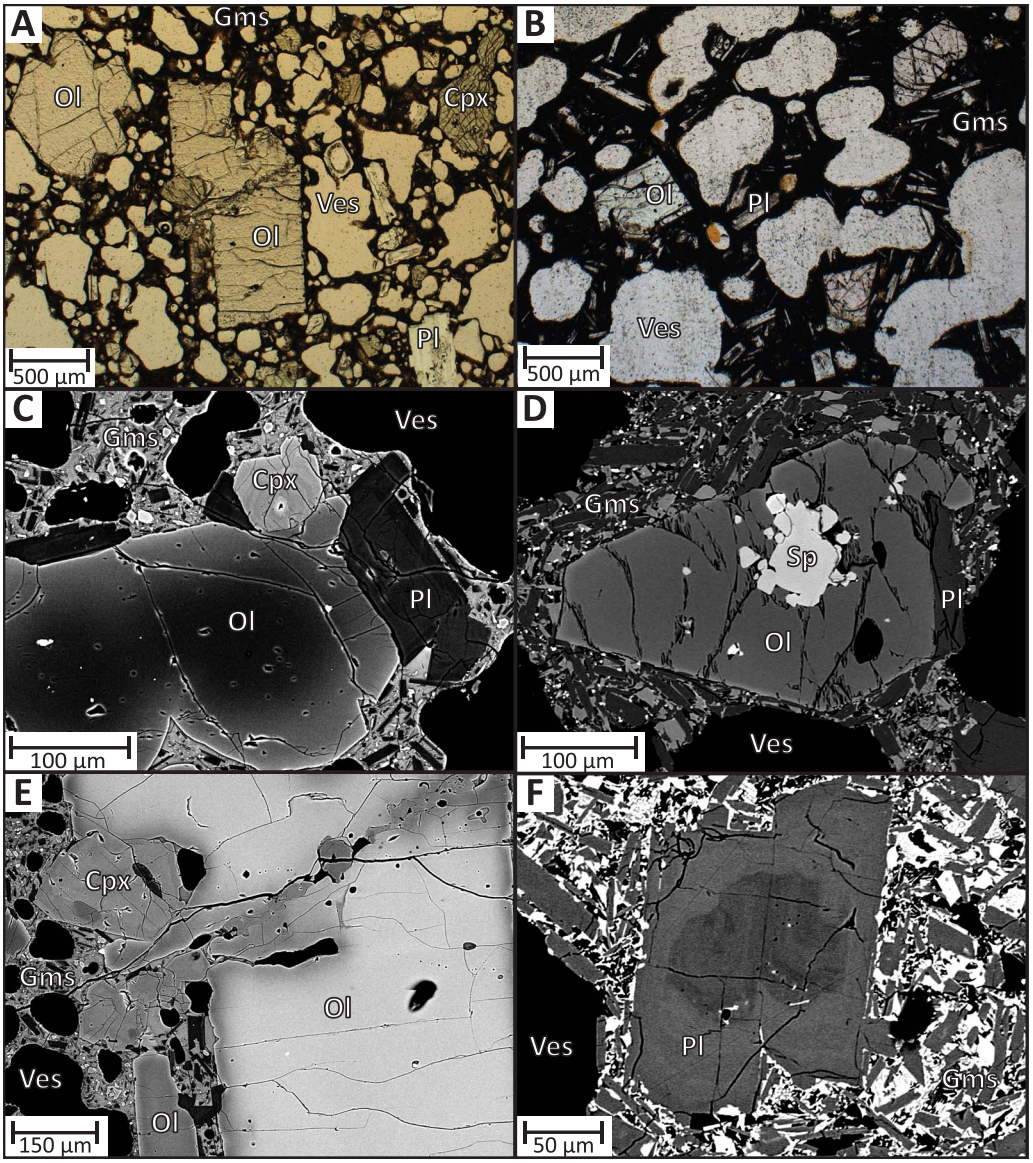

Fig. 2. Images of OO and RSH tephra samples. Plane-polarized light microphotographs of (A) OO and (B) RSH thin sections. BSE images of (C and E) OO, and (D and F) RSH samples.

component. All samples show LILE enrichment and the common Nb–Ta negative anomaly of subduction zone magmas.

The lowest Nb and Ta concentrations are found in HK, AKN and TT, followed by OO and AK, then TK, and the highest concentrations in RSH. The LILE abundances are lower in the NE Japan arc melts, followed by the Kuril arc melts, whereas the highest LILE concentrations are found in the back-arc samples. This increasing trend of LILEs seems to also be followed by increases in Rb/Ba and Th/Ba ratios. The Pb/Ce ratios are similar for all arc melts excepting TK, which has lower Pb/Ce ratios, followed by the back arc with the lowest Pb/Ce ratios.

Negative Zr anomalies are seen in all samples but the far back arc (RSH), and negative Ti anomalies are clearly seen in OO, TK and TT. In AK and HK only, some of the MIs show slight negative Ti anomalies. One OO MI, which corresponds to the group with very high Cl and F, has a different trace element pattern than the rest of the OO MIs. It is enriched in all trace elements compared to the other OO MIs, and it has a strong positive phosphorus anomaly. The positive Pb and Sr anomalies are not present in this sample as the LREE enrichment is stronger than the Pb and Sr enrichment.

The REE plots (Fig. 6b, d and f) show that LREE enrichment is low in AK, HK and TT (La/Yb between 1.7 and 2.1), slightly higher in TK and AKN (La/Yb between 2.2 and 3.3) and a lot higher in the back arc (La/Yb between 5.3 and 9.8). Slightly negative Eu anomalies are clear only in TK and TT.

Volatile elements

Measured volatile contents are shown in Figs 7 and 8. As with K_2O, Cl and F contents increase from NE Japan arc to Kuril arc, followed by TK and OO showing the highest Cl and F contents and a higher compositional range (*c.* 1500–*c.* 3800 µg/g Cl and *c.* 500–*c.* 1500 µg/g F). The RSH compositions follow a path of low Cl/F ratio, but with higher F contents than all arc front melts. All H_2O compositions are lower than 3.5 wt% and CO_2 contents are lower than 600 µg/g. New back-arc H_2O and CO_2 compositions overlap with the arc-front measurements given by Brahm *et al.* (2022), which range between *c.* 0.8 and *c.* 3.9 wt% H_2O and *c.* 29 to *c.* 426 µg/g CO_2 for OO and between *c.* 0.9 and *c.* 3.4 wt% H_2O and *c.* 15 to *c.* 524 µg/g CO_2 for RSH.

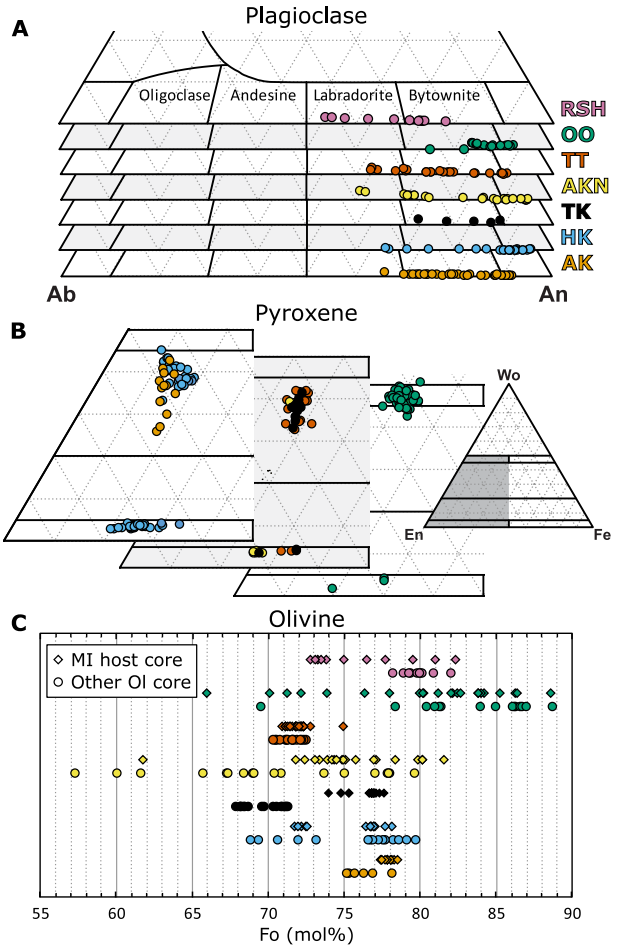

Fig. 3. Mineral compositions from EPMA analyses. (A) Plagioclase ternary plot with compositions from thin sections. (B) Pyroxene ternary plot with compositions from thin sections. (C) Olivine forsterite content of melt inclusion olivine hosts and olivine cores from thin sections.

As with the halogens, measured sulphur (S) concentrations are generally higher in the arc front samples than the back-arc samples. The arc front samples (excepting TK) range in S content from *c.* 300 to *c.* 2600 μg/g, whereas in the back-arc samples and TK, S contents range from *c.* 1480 to *c.* 4100 μg/g. Compositional ranges of S within each sample are generally wider than for Cl and F.

DISCUSSION

Post-entrapment corrections

The MIs of the arc front samples (AK, HK, TK, AKN and TT) were already assessed for post-entrapment processes in Brahm *et al.* (2022). Most arc front MIs showed evidence of being completely re-equilibrated to a constant Mg# during long storage histories, and post-entrapment crystallization (PEC) corrections applied reconstruct the compositions at the last equilibrium conditions during storage and not at entrapment. An attempt to apply the MushPEC algorithm (Brahm Scott, 2021) to estimate the compositions at entrapment was made by Brahm *et al.* (2022) but showed that the main differentiation process is boundary layer fractionation, precluding the derivation of primary MI compositions through MushPEC.

In contrast, the MIs from OO and RSH have Ol-host cores with a wider compositional range and without evidence of re-homogenization. PEC correction was applied using the following methodology. A modified MIMiC program was employed to obtain estimates of CO_2 contents before bubble formation using a calculated-volume approach to model the vapour-bubble growth (Rasmussen *et al.*, 2020; Brahm *et al.*, 2022). Host, MI and bubble dimensions were estimated the same way as done by Brahm *et al.* (2022). The modification of MIMiC consists of the implementation of the Papale *et al.* (2006) H_2O-CO_2 solubility model replacing the VolatileCalc model (Newman & Lowenstern, 2002), to maintain consistency with the corrected MIs from the arc melts.

The reverse Ol crystallization calculations were implemented using the Toplis (2005) model and the Putirka *et al.* (2007) Ol-melt thermometer. The initial H_2O content was estimated using the Gavrilenko *et al.* (2016) hygrometer model iteratively as in Brahm *et al.* (2022).

The iron speciation (Fe^{3+}/Fe_T) was estimated by calculating f_{O_2} conditions using the Sp-Ol oxybarometer of Nikolaev *et al.* (2016) and the iron speciation using Kress & Carmichael (1991). Temperatures used to derive the ΔQFM values were estimated from previous MIMiC runs at QFM. The calculated f_{O_2} conditions for OO are 0.85 ± 0.15 ΔQFM (from 12 Sp–Ol pairs) using temperatures of 1000–1100°C, and − 0.06 ± 0.18 ΔQFM (from 12 Sp–Ol pairs) using temperatures of 1080–1100°C.

Fe-loss (Danyushevsky *et al.*, 2000) was assessed for the PEC-corrected MIs. Most MIs of the OO and RSH samples follow the differentiation path of the whole rocks from the literature (Fig. 9) for OO (Katsui *et al.*, 1979; Katsui & Yamamoto, 1981; Yamamoto, 1988) and RSH (Katsui, 1953; Katsui *et al.*, 1978; Yoshida *et al.*, 1981; Ikeda *et al.*, 1990; Shibata & Nakamura, 1997; Kuritani, 1998; Ishizuka, 1999; Ishizuka & Nakagawa, 1999; Kuritani, 1999; Kuritani, 2001; Shuto *et al.*, 2004; Moriguti *et al.*, 2004; Kuritani *et al.*, 2005; Ishimoto *et al.*, 2006; Kuritani & Nakamura, 2006; Shimaoka *et al.*, 2016), with deviation towards lower FeO_T contents. The process of Fe-loss was corrected by adjusting the FeO_T content of corrected MIs to fit the MgO vs FeO_T trend of the whole rocks. The group of OO MIs with low Fo and reverse zoning shows a different level of Fe enrichment compared to the rest of the MIs and the main whole rock trend (Fig. 9a). These MIs are interpreted as xenocrysts which may have suffered complete Fe–Mg re-equilibration during long storage, increasing the FeO_T content of the MIs. Fe-loss correction was not applied to these MIs. All results of the PEC-correction models can be found in Appendix 4 of the supplementary material. The trends in Fig. 6 indicate that Ol was the only phase crystallizing during entrapment of most MIs of both samples. A group of MIs from RSH with the lowest MgO contents show a decrease in Al_2O_3 and CaO, indicating that Pl crystallization started at MgO contents of *c.* 5.5 wt%.

The corrected H_2O–CO_2 composition and estimated P–T (saturation pressure) conditions are shown in Fig. 7 and overlap with the values of the arc front melts from Brahm *et al.* (2022). The OO MIs show a wide range of H_2O contents between *c.* 3.2 and *c.* 9.3 H_2O, which translate into P and T ranges of *c.* 100–*c.* 450 MPa and *c.* 970–*c.* 1170°C, respectively. High Fe MIs have higher H_2O and P and lower T estimations. The PT range of OO MIs overlaps the range of all arc front MIs. The H_2O estimations of RSH MIs have a narrower range than those of OO (*c.* 4.4–*c.* 6.4 wt% H_2O), which also narrows down the P and T estimates (*c.* 120–*c.* 300 MPa and *c.* 1010–*c.* 1110°C, respectively).

Halogen and Sulphur loss

Halogen (Cl and F) contents of MIs are usually the best-preserved volatiles components in MIs, due to their high solubilities relative

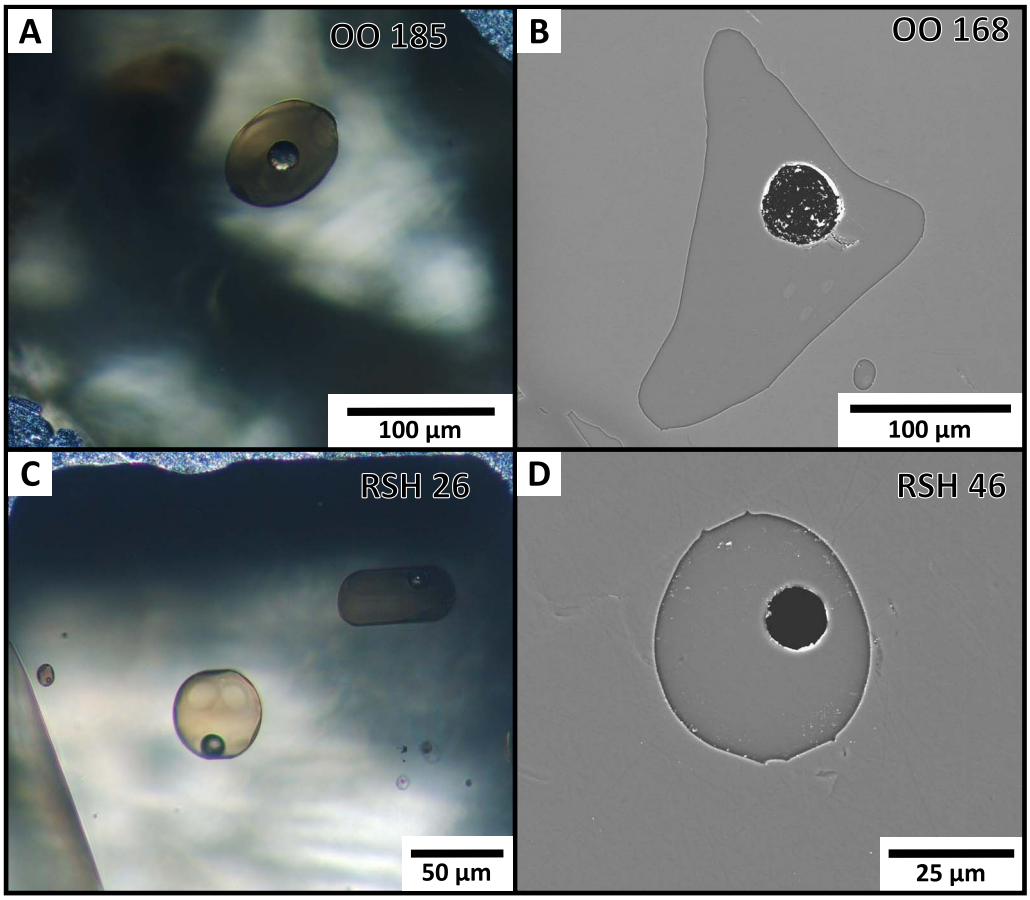

Fig. 4. Optic microscope (A and C) and BSE (B and D) images of representative OO and RSH olivine-hosted glassy melt inclusions.

to their abundance in basaltic melts (Carroll & Webster, 1994). Most of the samples in this study show a linear correlation between Cl and F, indicating a conservative behaviour, i.e. no loss of halogens after entrapment. Some of the samples present a wider variability in Cl and F ranges, not following a linear behaviour within the same sample. For example, AKN MIs have a group of low F contents for the same Cl range than the main group, following a linear trend with higher Cl/F ratio. Exsolution of Cl is an unlikely explanation for the Cl/F ratio variability in the AKN MIs, as other MIs in this study have up to four times more Cl than AKN MIs. It is likely that the variability in AKN Cl/F ratios is related to magma mixing, as the AKN tephra was composed of two very distinct fragment types (Brahm *et al.*, 2022). Interaction of different magma batches may also explain the few MIs from RSH with lower F contents. The highest halogen contents are found in OO MIs with a wider compositional range, where some MI compositions are displaced from the main Cl versus F trends towards higher F concentrations at *c.* 2000 µg/g Cl. This wide distribution of F compositions (*c.* 500–1500 µg/g F) at similar Cl contents is unlikely to be caused by Cl saturation as MIs with similar major element compositions have almost twice the Cl concentrations (up to *c.* 3800 µg/g). As the OO olivine compositions reach up to Fo_{89}, it is likely the MIs reflect melt compositions close to primary, trapped not long after mantle melting and without long storage times in shallow magmatic chambers. The halogen heterogeneity may reflect local variability of melting conditions before homogenization of the melts during storage.

As with H_2O and CO_2, sulphur has the potential to be exsolved from the melt before and after MI entrapment. The multiple oxidation states of S make its solubility behaviour strongly influenced by f_{O_2} conditions and sulphur can be affected by sulphate or sulphide mineral precipitation, immiscible liquid separation and degassing (e.g. Wallace & Carmichael, 1992; Moretti & Baker, 2008; Oppenheimer *et al.*, 2011; Ariskin *et al.*, 2013). After entrapment, S can be exsolved into the shrinkage bubble as a gas phase and/or precipitate minerals on the bubble boundary. The lack of reliable estimations of f_{O_2} conditions of the arc front melts make it difficult to estimate S solubilities, but studying the correlation of S concentrations with a known conservative element during magmatic fractionation and MI post-entrapment processes can help to identify S loss.

Figure 10 shows the concentrations of S and Cl. If the MIs within each sample are produced by the same slab fluid under similar conditions and S is behaving conservatively, the Cl versus S trends should follow a linear correlation that passes through the origin. The observed displacement to lower S concentrations for somewhat constant Cl contents observed in AK, TT, AKN, TK and RSH are thus interpreted to be caused by S loss. The highest S contents in MIs from AKN, TK, HK, OO and RSH appear to behave conservatively as they follow a line pointing towards the origin. Then, it can safely be interpreted that those S contents have not been affected by degassing. The S systematics of AK and TK do not show a conservative behaviour, indicating that the highest S content of each sample can be taken as a minimum initial S content. The MI from TT with the highest S is displaced from all other TT MIs, and it overlaps with the Cl/S ratio of HK and AKN. The highest S content of AK MIs has Cl/S ratios very similar to the rest of the arc front sample MIs (excepting TK). Therefore,

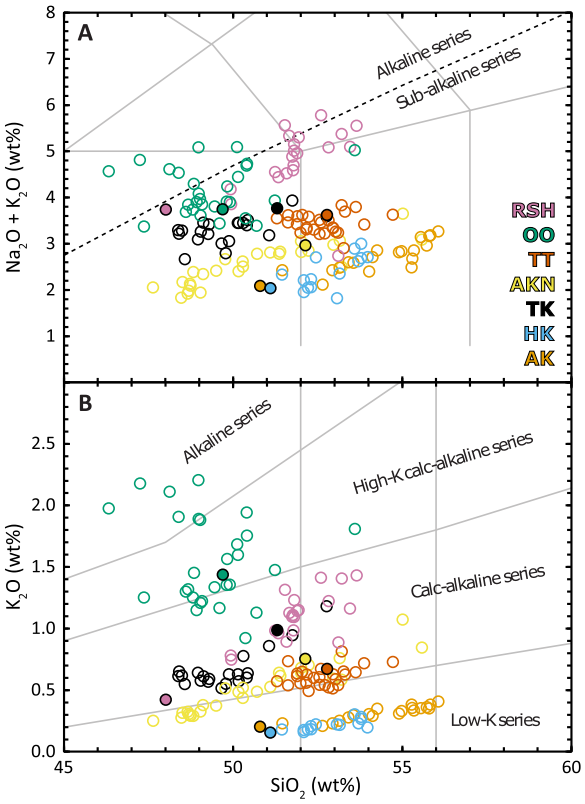

Fig. 5. Olivine-hosted melt inclusions and whole rock major element compositions of the seven tephra samples. Open circles are the melt inclusions and filled circles are the whole rock compositions. (A) TAS diagram. (B) K_2O vs SiO_2 diagram.

the original S contents in MIs of the arc front samples can be interpreted from the Cl concentrations and the estimated primary Cl/S ratios (*c.* 0.28–0.40), as it is observed in Fig. 10. The Cl/S ratios increase towards the back arc, with values of *c.* 0.45 for TK and *c.* 0.55–0.70 for OO. The Cl/S drops for RSH to *c.* 0.23 due to the Cl depletion observed in that sample.

Preservation of primary melt signatures

The recovery of primary melt compositions is key to the study of petrogenetic processes in subduction zones, which requires MIs hosted in forsteritic olivine (close to Fo_{90}). These MIs are preferred because they have suffered small amounts of fractional crystallization, usually only by crystallization of olivine, which is simple to correct for. Unlike primitive whole rock samples, primitive MIs contain some undegassed volatile components and are not affected by crystal accumulation. Despite the back-arc samples showing all these characteristics (OO and RSH), the arc front samples of this study are not all highly forsteritic (AK, HK, TK, AKN and TT), have suffered fractionation of multiple mineral phases and have suffered long storage histories. Thus, post-entrapment corrections are inaccurate and cannot be used to recover initial compositions. Nonetheless, some primary melt signatures are unaffected by all these processes. Ratios of conservative (incompatible) elements are not affected by processes other than mantle melting. In the following section these ratios are used to study across-arc variations and their relation to the metamorphic reactions occurring in the slab. These elements include most trace elements and halogens. Notable exceptions are Sr and Eu (affected by plagioclase fractionation) and Ti (affected by Fe–Ti oxide fractionation).

Correlation between trace/volatile signatures and slab conditions

Studies of natural high grade metamorphic suites from old subduction systems (Sorensen *et al.*, 1997; John *et al.*, 2011; Martin *et al.*, 2014; Pagé & Hattori, 2017), dehydration and melting experiments of basaltic and pelitic rocks (Schmidt & Poli, 1998; Hermann & Green, 2001; Kessel *et al.*, 2005; Hermann & Rubatto, 2009; Dalou *et al.*, 2012; Krenn *et al.*, 2012) and thermodynamic modelling (Connolly & Kerrick, 1987; Connolly & Petrini, 2002) have enabled the prediction of the mineralogical composition of the slab and the partitioning behaviour of trace elements, whereas geodynamic models (Syracuse *et al.*, 2010) have allowed the estimation of slab PT paths for subduction systems worldwide.

Figure 11 summarizes the expected stability fields of relevant hydrous minerals in the different layers of the slab under the estimated PT conditions of the slab surface below each volcano. Correlations between prograde metamorphic reactions and trace element ratio variations are studied using this plot. Uncertainties of the estimated PT conditions are difficult to estimate as they involve the combination of different models. Also, corner flow in the mantle wedge may play an important role in displacing the location of the volcano with respect to the location of slab component release. Nonetheless, as most of the uncertainties as well as the corner flow affect the estimations of each volcano similarly, the relative difference between PT estimates of the slab below each volcano is expected to be more accurate. Then, across-arc variations may be correlated with the progressive metamorphic reactions in the slab as PT conditions increase towards the back arc. The vertical pressure increase from the slab surface to the Moho is estimated to be less than 0.2 GPa. This indicates that the conditions below the slab surface for each volcanic unit can be approximated by a sub-horizontal line in Fig. 11 (almost constant P for the whole T range).

The PT paths of each slab layer surface were taken from the lookup tables in the Arc Basalt Simulator version 5 spreadsheet (Kimura, 2017), which were obtained by the models D80 of Syracuse *et al.* (2010). The models selected correspond to the N Honshu and S Kuril sections. Conditions between 6 and 8 GPa were obtained by a quadratic extrapolation based on the shape of the curves at high pressures (*c.* 4–6 GPa). This is due to the lack of PT path data above 6 GPa in the Arc Basalt Simulator spreadsheet, which increases uncertainties of the PT path models. However, small variations in the conditions of the slab below RSH do not affect the interpretations of the present study.

The conditions of the slab below each volcanic system were estimated by combining the information of crustal depth (CRUST1.0) (Laske *et al.*, 2013), slab depth (Slab2) (Hayes *et al.*, 2018) and slab surface P–T path models (Syracuse *et al.*, 2010). Using values of crustal and mantle densities from the CRUST1.0 model, the pressure of the slab below each volcanic system is estimated, and the slab P–T path model indicates the temperature of the slab surface. Estimated conditions are summarized in Table 1.

Stability fields and H_2O content at saturated conditions for DMM (Workman & Hart, 2005) and MORB (Moyen & Stevens, 2006; Hacker, 2008) were calculated with Perple_X version 6.9.1 (Connolly & Kerrick, 1987; Connolly & Petrini, 2002) for sub-solidus conditions, using the hp62ver.dat data file (Holland & Blundy, 1994; Green *et al.*, 2016). Stability fields at sub-solidus and super-solidus conditions, H_2O at saturation, and melt proportion of SED (pelite) (Hacker, 2008) for the range of 1–6 GPa was taken from the lookup tables in the Arc Basalt Simulator version 5 spreadsheet, which combines Perple_X calculations for sub-solidus conditions

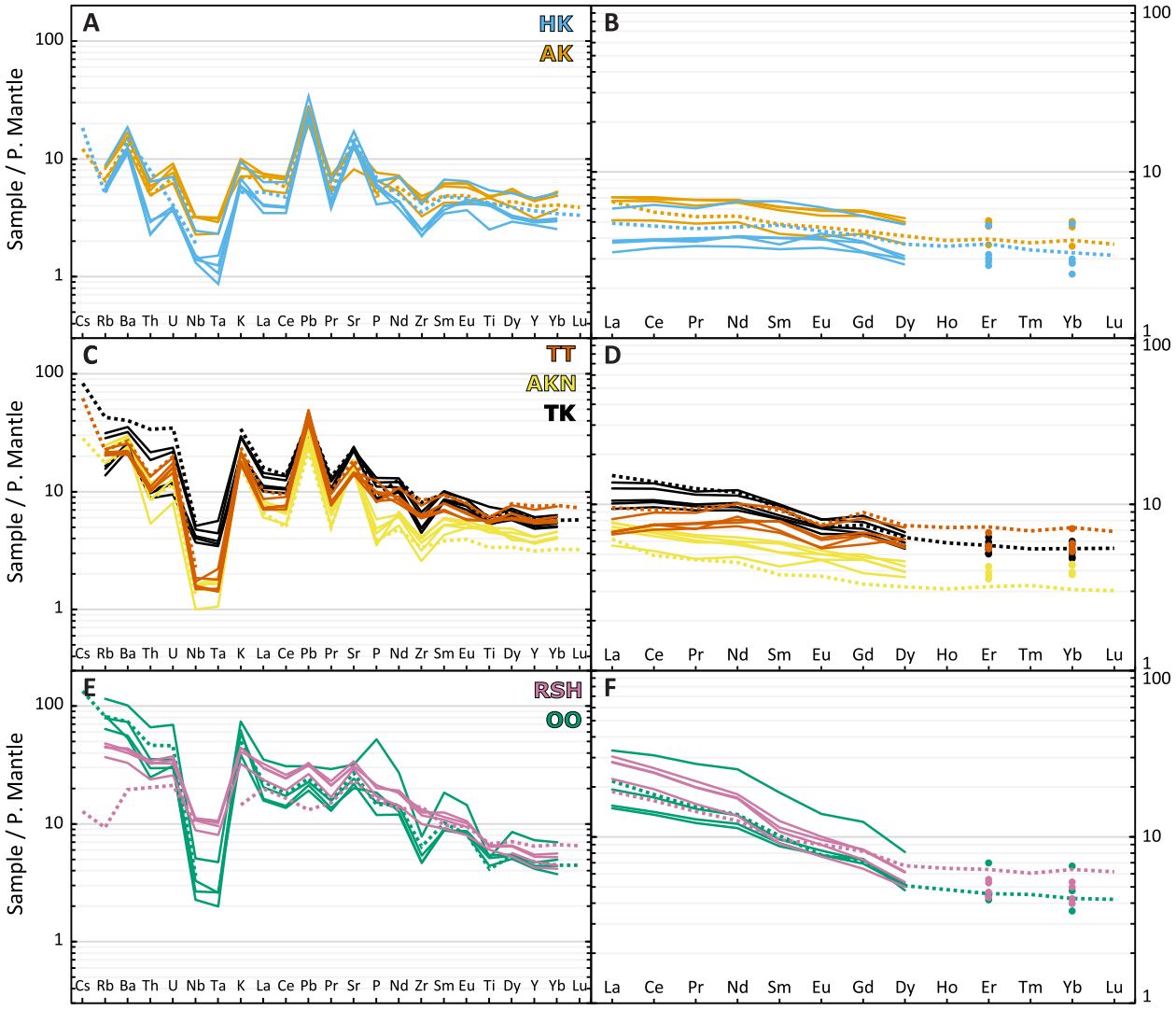

Fig. 6. Spider and REE diagrams of LA ICP-MS measured melt inclusions compositions (continuous lines) and whole rock samples (dotted lines).

Table 1: Estimated slab surface conditions below each volcano

Volcano	Slab depth (km)	P (GPa)	T (°C)
AK	91	2.7	710
HK	93	2.8	719
OO	165	5.1	812
TK	125	3.7	766
AKN	93	2.8	695
TT	104	3.1	739
RSH	252	7.8	869

with experimental results (Schmidt *et al.*, 2004; Hermann & Spandler, 2008) for the solidus–liquidus interval. The simplified SED composition used in this model should be close enough to what it is expected for the sediments found in these subduction zones. Both trenches in Northern Honshu and the southern Kuril consist mainly of diatom clays and pelagic clays of similar thickness (Plank, 2014).

Trace elements

Across-arc variations of trace element ratios can be visualized in Fig. 12. Ratios of fluid immobile high-field strength elements (HFSEs; e.g. Nb/Yb, Zr/Yb) are affected by the composition of the mantle source and the degree of melting. AKN and TT compositions are consistent with a depleted mantle source (DMM), whereas HK, AKN, TK and OO are consistent with different melting degrees of a more enriched source (E-DMM) (Fig. 12a). The higher Nb/Yb and Zr/Yb ratios of the far back arc (RSH) are consistent with low degree melting of a garnet-bearing source, but this is inconsistent with the flat MREE to HREE trend in Fig. 6d (Dy/Yb < 2). This suggests mobilization of HFSE from the slab caused by a supercritical nature of the slab liquid above 6 GPa under RSH (Schmidt *et al.*, 2004; Kessel *et al.*, 2005; Taniuchi *et al.*, 2020), and the resulting dissolution of the main HFSE carriers (rutile and zircon) at high T_{slab} (Hermann & Rubatto, 2009).

Ratios of elements with similar solid/melt partitioning behaviour but contrasting solid/fluid partitioning behaviour, like Pb/Nb and Ba/Nb, are commonly used to study differences in slab input in arc magmas (e.g. Moriguti *et al.*, 2004). These ratios are only weakly affected by variations in melting conditions, but strongly affected by the amount and composition of the slab component. Nonetheless, a homogeneous mantle source composition needs to be assumed to draw any conclusions about variations of slab input, as Nb is strongly affected by the degree of source depletion. The Nb/Yb ratios are indicative of a variable

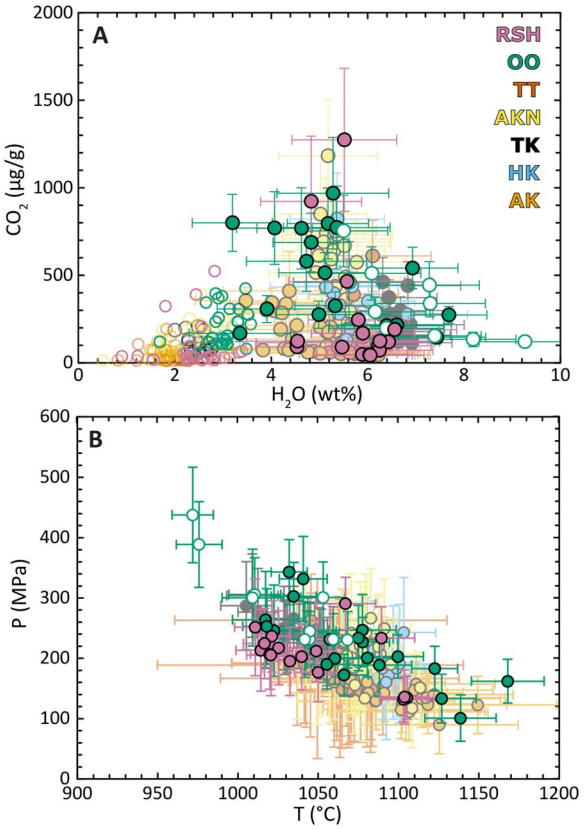

Fig. 7. (A) Measured (hollow circles) and corrected (filled circles) H2O and CO_2 contents and (B) PT estimated conditions of melt inclusions for OO and RSH, overlayed on data of arc front melt inclusions from Brahm *et al.* (2022). Error bars are 1σ. White circles with coloured outline correspond to the Fe-rich melts from xenocrystic olivine hosts form OO (see below).

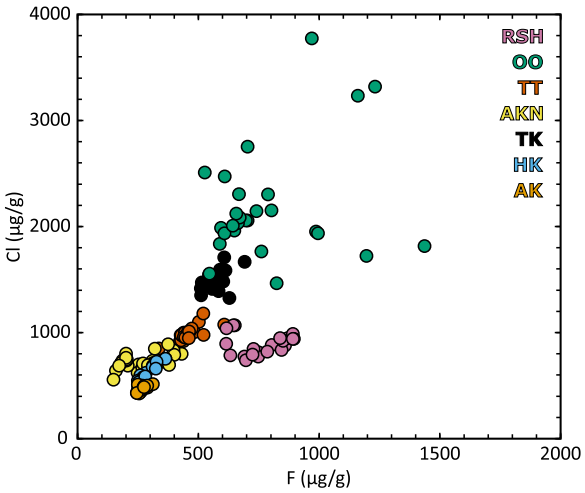

Fig. 8. F and Cl compositions of the melt inclusions from all samples. Uncertainties (1σ) are similar to the circle diameter.

source composition and Nb enrichment in RSH, complicating inferences of slab component variations from ratios like Pb/Nb (Fig. 12b). Here, Yb as a denominator is preferred, as ratios are less affected by source composition and moderately affected by melting degree. This allows a qualitative interpretation of across arc changes that are beyond the ranges explained by melting degree variations.

The LREE/Yb ratios, represented by La/Yb in Fig. 12d, show overlapping values within the lower slab surface temperature (T_{slab}) arc front melts, followed by a steady increase from *c.* 2 in TT to *c.* 6–10 in RSH. The LREE/Yb ratio increases slightly with degree of source enrichment and lesser degrees of partial melting, but not to the extent of LREE enrichment observed in the back arc. The observed steady increase in LREE towards higher T_{slab} is therefore more likely produced by the sequential and temperature-dependent dissolution of LREE-rich accessory phases (e.g. allanite) (Klimm *et al.*, 2008; Hermann & Rubatto, 2009). Allanite is expected to be present as a residual phase up to T_{slab} of *c.* 850–900°C, which includes the whole range of conditions across arc from AKN to RSH.

The LILEs, in addition to U and Th, are divided into two groups of distinct behaviour: (group 1) Rb, Ba, K, U and Th and (group 2) Pb and Sr. The Ba/Yb ratios representing group 1 (Fig. 12e) decrease from *c.* 100 to *c.* 50 from AKN to AK, and then increase towards OO (*c.* 200), dropping to *c.* 100 in RSH. The main carrier of Ba in the oceanic crust and sediment cover is phengite (Tamura *et al.*, 2007; Hermann & Rubatto, 2009) and phengite breakdown progresses with melting of the sediment as temperature increases. However, the sediment PT path indicates that melting is not expected to increase towards the back arc (Fig. 11), as the solidus line intersects the PT path of the sediment cover towards the back arc, making it an unlikely source of LILE across-arc enrichment. In addition, the model in Fig. 11 does not account for progressive melting of the sediment layer, which would hinder the sediment melting across arc even more. Also, LILE variations within arc front conditions or along-arc variations that can be affected by changes in the sediment layer along the trench cannot be assessed by our data, as the variations are within ranges affected by melting degree (Fig. 12e).

Another source of LILE in the arc front can be amphibole and chlorite from the hydrated mantle wedge above the slab, which was hydrated in the forearc and dragged down by the corner flow. These phases can supply part of the LILE budget in the arc front but are no longer present towards the back arc (at higher PT conditions than TT in Fig. 11). Serpentine (antigorite in Fig. 11) is the main carrier of these LILE in the hydrated lithospheric mantle (Scambelluri *et al.*, 2004). The hydrated mantle can transport more than 11 wt% H_2O mainly as antigorite and chlorite (Fig. 11), and this water is released with progressive breakdown of this phases as PT conditions increases. The antigorite stability limit is roughly placed at the pressure of the lithospheric mantle beneath OO volcano, indicating that an elevated slab component signal towards the back arc occurs by increasing participation of the lithospheric mantle in the release of fluids from the slab (Straub & Layne, 2003; John *et al.*, 2004; Barnes *et al.*, 2008; Herms *et al.*, 2012; John *et al.*, 2012; Konrad-Schmolke & Halama, 2014; Martin *et al.*, 2016; Yamada *et al.*, 2019; Martin *et al.*, 2020). The potential of slab fluid enrichment in back-arc magmas would then be controlled by the level of hydration of the lithospheric mantle, which occurs during normal faulting of the outer rise (Ranero *et al.*, 2003; Faccenda *et al.*, 2008; Cai *et al.*, 2018; Grevemeyer *et al.*, 2018). Furthermore, hotter subduction zones have a higher potential to release fluid compared to colder subduction zones (Syracuse *et al.*, 2010), as colder subduction zones can retain up to *c.* 4 wt% H_2O in the alpha-phase beyond 8 GPa (Fig. 11). The decrease in Ba/Yb ratios observed for RSH melts reflects exhaustion of antigorite and chlorite. Higher Ba/Yb ratios at the lowest T_{slab} samples in the arc front melts are within ranges explained by the degree of melting. However, AKN MIs show no enrichment in other mobile elements with respect to the rest of arc front samples, so it is more likely

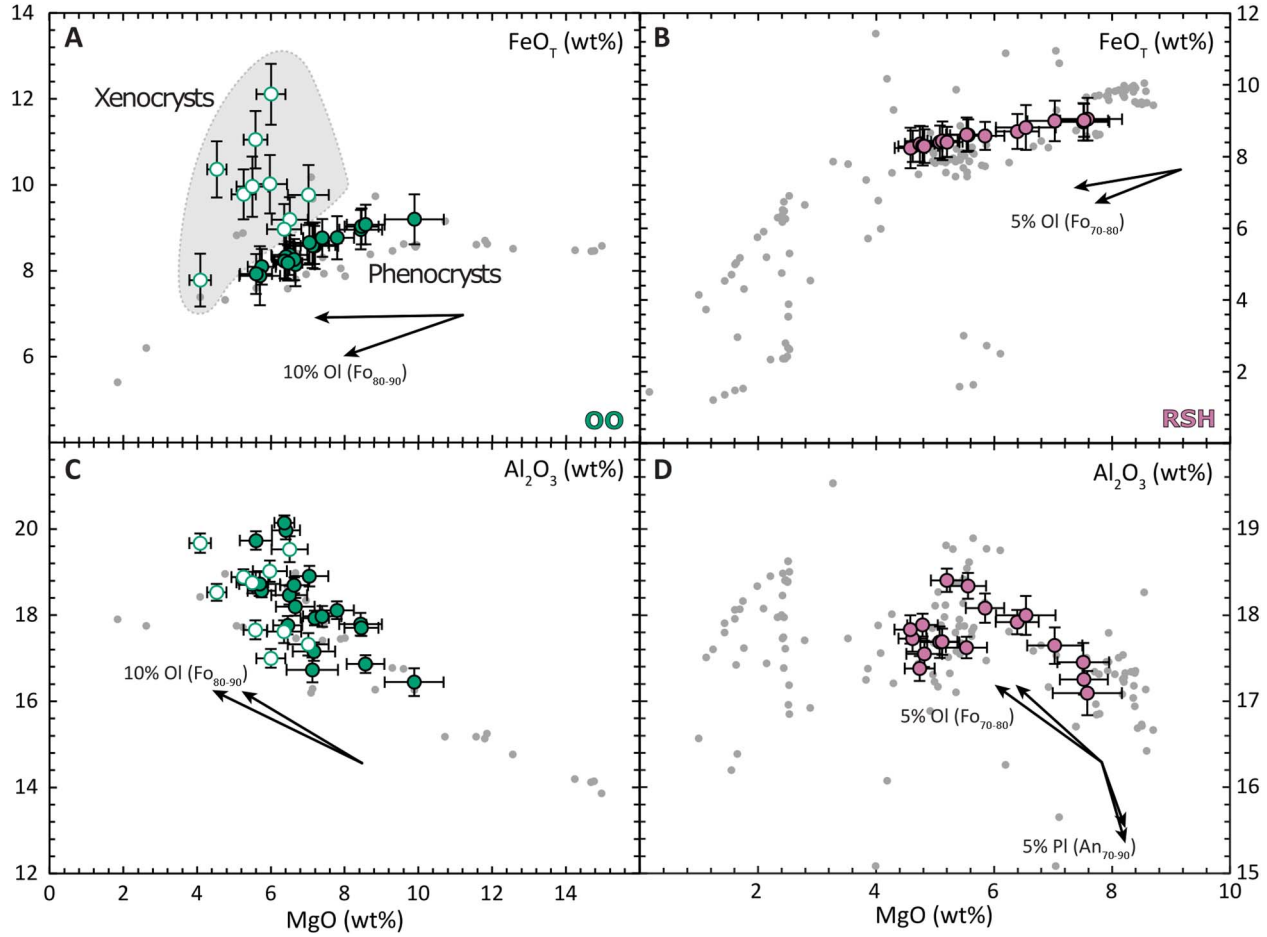

Fig. 9. Variation diagrams of melt inclusions from (A and C) OO and (B and D) RSH, corrected for post-entrapment crystallization and Fe-loss processes. Error bars indicate 1σ uncertainties. Small dots are whole rock data from literature (see main text). White symbols with coloured outlines in (A) and (C) correspond to melt inclusions hosted in high-Fo olivine of OO interpreted as xenocrysts. Arrows indicate the fractionation models of olivine and/or plagioclase. The two arrows for each phase indicate the compositional variation of the respective phase.

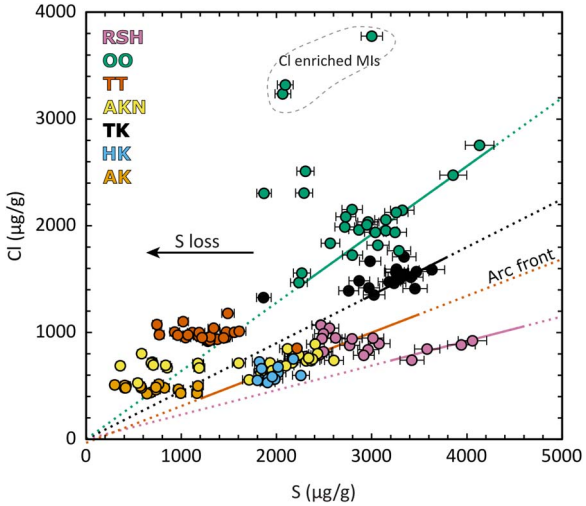

Fig. 10. Measured Cl and S compositions of the melt inclusions. Dotted lines indicate the approximated Cl/S ratios for the different samples before S loss and the continuous lines indicate the range of corrected S concentrations of each sample.

that Ba/Yb enrichment reflects a slab component with higher Ba. This may be related to the nature of the slab component. The spikes of Ba/Th values observed in the samples with low T_{slab} (AKN and HK; Fig. 12f) indicate the participation of an aqueous fluid phase, whereas the lower Ba/Th ratios at slightly higher T_{slab} argues for the participation of a silicate melt in the slab component (Kessel *et al.*, 2005; Pearce *et al.*, 2005).

The LILEs of group 2 (Pb and Sr), represented by Pb/Yb ratios in Fig. 12c, do not vary significantly between arc and back arc (*c.* 1–3), with ratios that are within a range that can be explained by differences in the degree of melting. The main carrier of Pb and Sr is lawsonite and zoisite (Spandler *et al.*, 2003; Feineman *et al.*, 2007; Martin *et al.*, 2011; Martin *et al.*, 2014). Zoisite is not predicted to be present in oceanic crust in the model of Fig. 11, but experiments by Forneris & Holloway (2003) equilibrated zoisite at PT up to *c.* 3 GPa and 650°C, which is only relevant for the lower-T arc front samples. In contrast, lawsonite is present in the oceanic crust and stable to great depths (Schmidt & Poli, 1998). Steady across-arc breakdown of lawsonite provides a constant supply of Pb and Sr, including below RSH. Any increase Pb and Sr supplied from the lithospheric mantle will be buffered by the lawsonite-bearing layer above it. Any additional Pb released at arc front depths by zoisite breakdown would be also buffered by the presence of lawsonite.

Volatile elements

The Cl/Yb ratios behave similarly to Ba/Yb ratios, whereas F/Yb ratios increase to a lesser degree towards OO with similar values

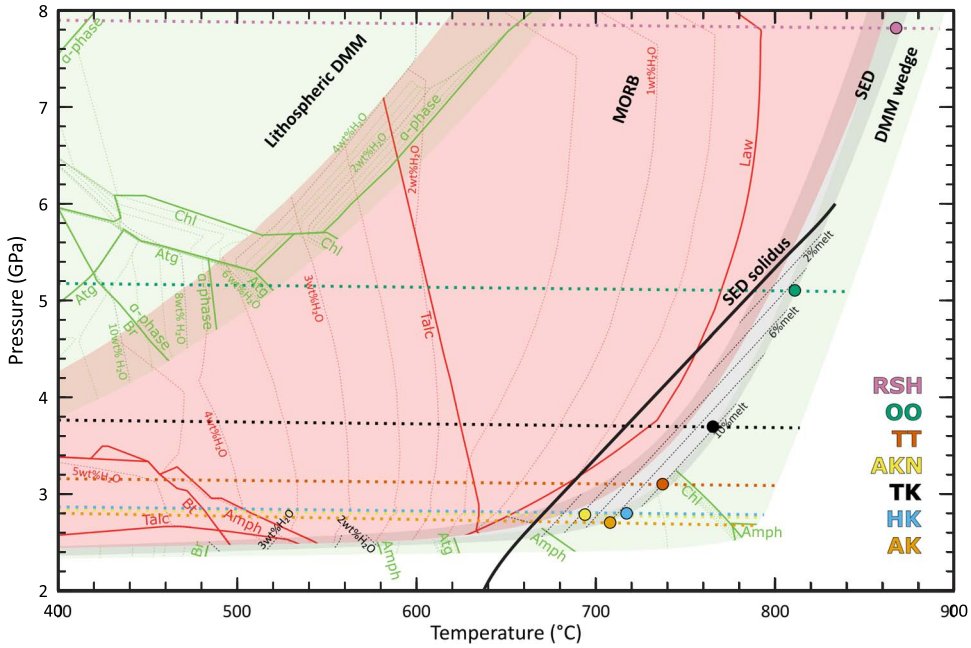

Fig. 11. PT paths of slab layers with stability fields of hydrous mineral phases and the amount of water at saturation. Detailed explanation of the construction of this plot can be found in the main text. Shaded fields indicate the different lithologies of the subducted slab. From top left to down right these are: lithospheric depleted mantle (DMM), altered oceanic crust (MORB), sediment cover (SED) and DMM wedge. The thick continuous line indicates the wet solidus of the sediment cover. Continuous coloured lines indicate the stability limits of hydrous phases. Hashed coloured lines indicate H_2O isopleths and hashed black lines in the SED field indicate the sediment melting degree. Coloured circles indicate the estimated PT conditions of the slab surface below each volcano and dotted lines of same colours are indicate the estimated PT conditions at all layers of the slab (colour scheme as in Fig. 1). Atg = antigorite, Chl = chlorite, Amph = amphibole, Br = brucite, α-phase = alpha phase, Law = lawsonite, Bt = biotite.

in RSH. Both Cl and F are carried by antigorite (John *et al.*, 2011; Kendrick *et al.*, 2020), but Cl has been shown to be more fluid mobile than F (Bernini *et al.*, 2012), producing a higher Cl enrichment. Also, F enrichment has been observed in subducted lawsonite (Pagé *et al.*, 2016), causing F retention as exhibited by fluids percolating through the oceanic crust, but this implies lawsonite is also a source of F-enriched fluid during its breakdown. Thus, lawsonite controls F enrichment or depletion (Fig. 12h). All these results show that even though the LILE and halogen budgets in the arc front are strongly controlled by the sediment cover (Patino *et al.*, 2000), across arc trends indicate that variations (or the absence of variations) in these elements are controlled by reactions occurring in the oceanic crust (lawsonite breakdown) and the lithospheric mantle (antigorite breakdown). The OO MI with the highest F corresponds to a trace element pattern enriched in both P and REE, which is consistent with apatite breakdown in the slab source.

The increase of Cl towards the back arc can be caused either by an increase in the salinity of the slab liquid and/or an increase in the proportion of slab liquid in the primary melt. The coupled across-arc variations of Cl and LILEs of group 1 can also be explained by both options. Experiments from Rustioni *et al.* (2021) showed a consistent increase of LILE mobility in the fluid with salinity increase. As we could not recover reliable H_2O contents of the primary melts from the MIs, it is hard to assess if the increase of Cl and LILE is directly tied to an increased amount of fluid. Rustioni *et al.* (2021) also found that LREE have the same increase in fluid/eclogite partitioning with salinity, which could also explain the LREE increase towards the back arc as an alternative to allanite dissolution. Nonetheless, the continued increase of LREE towards the far back arc (RSH) despite the drop in Cl is consistent with the temperature-controlled allanite dissolution without considerable changes in the salinity of the slab liquid, making the increase of slab liquid proportion a more probable cause for the Cl and LILE changes across arc.

Walters *et al.* (2020) modelled the release of sulphur in the slab fluid from the AOC as subduction progresses in the arc front for the Honshu PT path (Syracuse *et al.*, 2010) using Perple_X. The main reaction affecting the S budget at these conditions is progressive pyrite oxidation forming anhydrite, which releases oxidised S species (HSO_4^- and SO_4^{2-}). These species, transported in the slab liquid to the mantle source, are believed to be the main oxidation agents in arc magmas (e.g. Kelley & Cottrell, 2009; Evans *et al.*, 2012; Muth & Wallace, 2021; Muth & Wallace, 2022). S solubility in rhyolitic melts produced by sediment melting under conditions relevant for arc front depths has shown to be high under reduced and oxidized conditions (Li *et al.*, 2021; Muth & Wallace, 2022), where minimum solubilities are found at oxygen fugacities of *c.* QFM + 1, increasing towards lower and higher f_{O_2} conditions.

The constant Cl/S observed in the arc front (Fig. 10) indicates that the fluid composition released along the arc has the same S and halogen contents, suggesting that these sulphide oxidation reactions in the slab at arc front depths are similar along the NE Japan arc and Kuril arc. This suggests similar degrees of alteration, oxidation states, sulphide/sulphate contents of the oceanic crust and sediments for both arcs. The S content variation within arc front melts then follows the same behaviour as seen for the halogen contents and can be related to the amount of slab liquid in the primary melt.

The higher amounts of S towards the back arc can be tied to serpentine breakdown. The antigorite breakdown reaction produces a highly oxidized fluid (Debret & Sverjensky, 2017), which enhances the mobility of sulphur, as sulphides buffer the oxidation process through dissolution of S into oxidised species. In addition, salinity increase produced by Cl released from

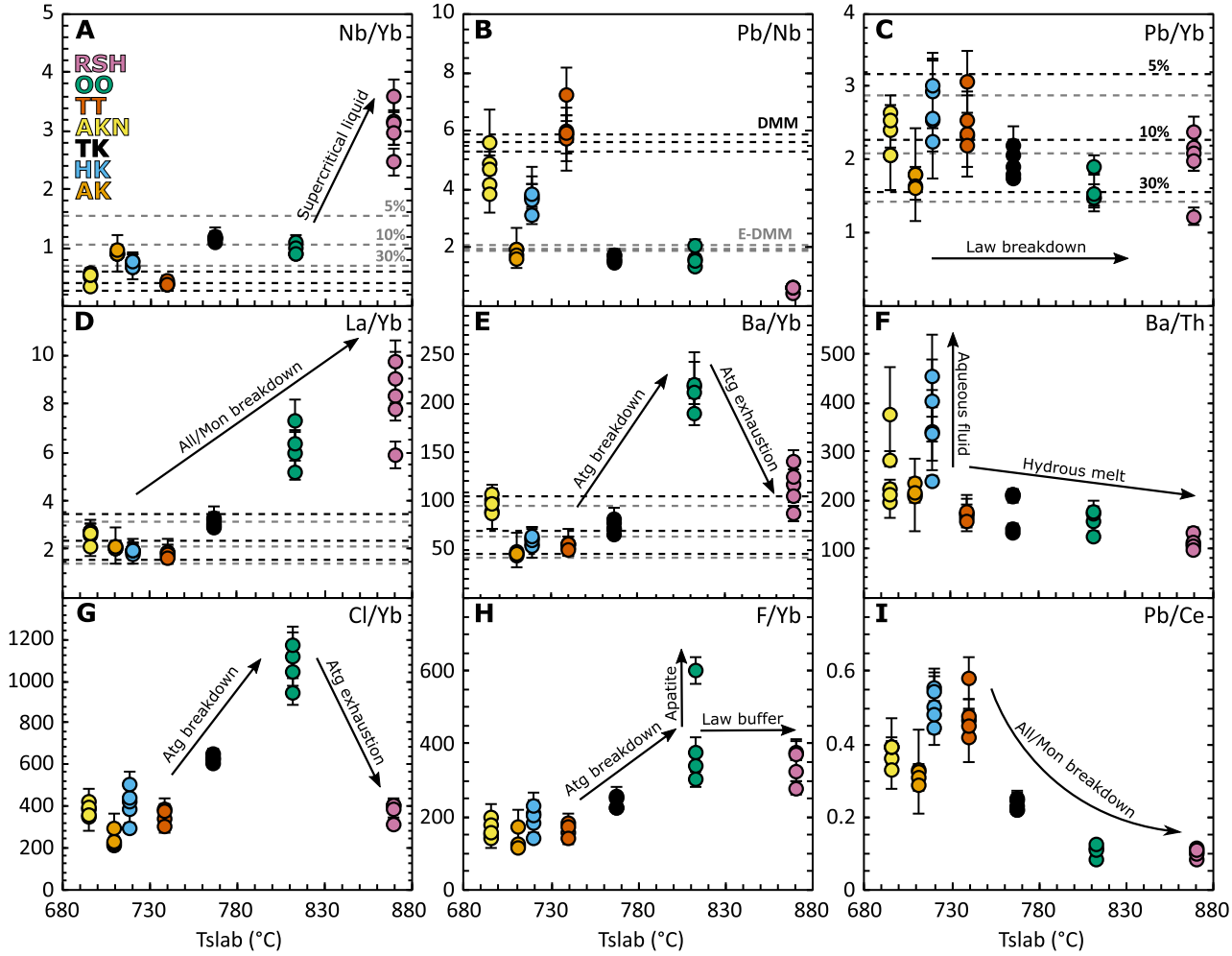

Fig. 12. Variation of elemental ratios of melt inclusion data with estimated slab surface temperature below each volcanic system (T_{slab}). Error bars indicate 1σ uncertainties. Arrows with text indicate the processes causing the observed trends (see main text). Dashed lines indicate batch melting models (5, 10 and 30%) for DMM (black) and enriched DMM (grey) (Workman & Hart, 2005) doped in Pb, Ba and La. See the supplementary material for details on these models.

serpentine also enhances sulphur mobility (Newton & Manning, 2005). The higher Cl/S ratios in TK and OO appear to be caused by a higher increase of Cl than S from the serpentine breakdown at these locations. In addition, melting experiments have shown that S solubility (as sulphur content at sulphide saturation, SCSS, or at anhydrite saturation, SCAS) increases with temperature (Prouteau & Scaillet, 2012; Jégo & Dasgupta, 2013; Jégo & Dasgupta, 2014), consistent with increased S contents in back-arc melts.

The higher S contents in RSH than at the arc front, despite serpentine exhaustion, which stops the production of highly oxidized saline fluids, might be related to the dissolution of sulphides or sulphates at these PT conditions or enhanced mobility of S in supercritical fluids. Wallace (2005) predicts that significant amounts of S survive slab dehydration/melting at arc/back-arc depths and return to the deep mantle. This indicates that significant amounts of S carrier phases are still present at c. 8 GPa in the slab, providing a source of S to RSH.

Comparison with other across-arc studies

Across-arc geochemical studies have been previously conducted in Japan and other island and continental arcs, some drawing opposite conclusions than the present study. We believe that in many cases, these contrasting results were caused by the use of LILE/Nb and LILE/LREE ratios. For example, Moriguti *et al.* (2004) used Pb/Nb ratios of whole rock samples from some of the same volcanoes studied here, predicting a steady decrease of slab input from arc to back arc. Other researchers (Walker *et al.*, 1995; Patino *et al.*, 1997; Churikova *et al.*, 2001; Wade *et al.*, 2006; Sadofsky *et al.*, 2008; Jacques *et al.*, 2013; Wehrmann *et al.*, 2014; Bénard *et al.*, 2018) have used LILE/LREE ratios (*e.g.* Pb/Ce in Fig. 4i), commonly taken as proxies of fluid input in arc settings. Our work suggests that caution should be taken when using these ratios as slab tracers. The present study shows a strong effect of source composition on LILE/Nb slab proxies and also suggests that LILE/LREE ratios may not be appropriate slab tracers when studying across-arc variations due to possible LREE enrichment as T_{slab} increases. The interpretation of decreasing slab input due to observed decreases in these ratios across arc may have to be reassessed.

Other across-arc studies of island arcs show results similar the present study. For example, Tollstrup *et al.* (2010) analysed across arc trace element variations of volcanic glasses in the Izu-Bonin arc. The LREE/Yb ratios show enrichments from arc front to back arc similar to this study (c. 4 times higher La/Yb ratios in the back arc). This agrees with the T-dependent dissolution of allanite. There is a lot of spread in the across arc variations of Ba/Yb, but with a general increase towards the back arc, agreeing with an increase of a fluid-rich lithospheric mantle component with subduction depth. The Pb/Yb mostly overlap across arc, agreeing

with lawsonite buffering in the oceanic crust. There are some higher Pb/Yb ratios in the arc front, which may be explained by Pb-rich fluids extracted from the sediment cover.

In contrast to the case of island arcs, represented by the previous example and the present study, across-arc variations in continental arc settings do not show the same increase in trace elements. Across-arc variations in Central America (Honduras; Patino *et al.*, 1997) and the Southern Andes (Chile; Jacques *et al.*, 2013) show no enrichment in LILE towards the back arc. Ba/Yb ratios in Honduras and Pb/Yb ratios in Chile decrease across arc, indicating that there is no increase in participation of the lithospheric mantle as source of fluid towards the back arc. This contrasting behaviour may be caused by the level of fracturing of the slab and hydration of the lithospheric mantle in the outer rise. Slab dip angles in Central and South America are lower than in Japan and the Izu-Bonin, which translate into lesser bend and fracturing of the oceanic crust in the outer rise, reducing the degree of lithospheric mantle hydration and hindering the transport of fluids across the slab column during dehydration. In particular, the case of LILE enrichment towards OO in the present study may be additionally aided by the bending of the slab due to the change of the trench strike from the Kuril to the NE Japan subduction (Fig. 1). This bending causes fracturing and/or thinning of the slab, facilitating the transport of fluids sourced from the lithospheric mantle (Kuritani *et al.*, 2014).

CONCLUSIONS

Compositional variations in natural samples across an arc setting track the prograde metamorphic reactions in the various components of the subducting slab. It can thus be used to infer source processes. However, the present study also highlights the inaccuracy of LILE/LREE and LILE/Nb ratios as fluid proxies when comparing arc and back arc melts or melts from different mantle source compositions.

The geochemical variations of olivine-hosted MIs also record changes in the nature of the slab fluid with increasing PT conditions of the slab. A transition from an aqueous fluid to a hydrous silicate liquid is evidenced by a substantial decrease of Ba/Th ratios at arc front conditions. A transition to a supercritical liquid is inferred for the back arc at P of *c.* 8 GPa due to the observed increased mobility of the HFSE. The LILE and halogens evidence an enhanced participation of the hydrated lithospheric mantle (antigorite breakdown) in the fluid release towards the back arc. Depletion of Ba and Cl in the volcano farthest from the trench (RSH) agrees with exhaustion of antigorite as a fluid source. The fluid budget towards the back arc is then controlled by the level of hydration of the lithospheric mantle and the facilitation of upward transport of the released fluids through the slab by its faulting in the outer rise, which is consistent with the differences found between high angle (Japan, Izu-Bonin) and low angle (Central and South America) subduction settings.

ACKNOWLEDGEMENTS

We thank Ian Schipper for help with the EPMA work at Victoria University, Amanda French for help with LA ICP-MS analysis at the University of Waikato and Mark Kendrick for providing the glass reference materials for volatile analysis. This research and the PhD scholarship to RB were funded by the Royal Society of New Zealand through the Marsden Fund (grant MAU1704 to GFZ). We also want to acknowledge the work of the referees and Associate Editor, Prof. Reto Gieré, for their comments that helped improved this work.

SUPPLEMENTARY DATA

Supplementary data are available at *Journal of Petrology* online.

DATA AVAILABILITY

The data underlying this article are available in the article and in its online supplementary material.

References

Acocella, V., Yoshida, T., Yamada, R. & Funiciello, F. (2008). Structural control on late Miocene to quaternary volcanism in the NE Honshu arc, Japan. *Tectonics* **27**. https://doi.org/10.1029/2008TC002296.

Ariskin, A. A., Danyushevsky, L. V., Bychkov, K. A., McNeill, A. W., Barmina, G. S. & Nikolaev, G. S. (2013). Modeling solubility of fe-ni sulfides in basaltic magmas: the effect of nickel. *Economic Geology* **108**, 1983–2003. https://doi.org/10.2113/econgeo.108.8.1983.

Barnes, J. D., Sharp, Z. D. & Fischer, T. P. (2008). Chlorine isotope variations across the Izu-Bonin-Mariana arc. *Geology* **36**, 883–886. https://doi.org/10.1130/G25182A.1.

Bénard, A., Klimm, K., Woodland, A. B., Arculus, R. J., Wilke, M., Botcharnikov, R. E., Shimizu, N., Nebel, O., Rivard, C. & Ionov, D. A. (2018). Oxidising agents in sub-arc mantle melts link slab devolatilisation and arc magmas. *Nature Communications* **9**, 3500. https://doi.org/10.1038/s41467-018-05804-2.

Bernini, D., Wiedenbeck, M., Dolejš, D. & Keppler, H. (2012). Partitioning of halogens between mantle minerals and aqueous fluids: implications for the fluid flow regime in subduction zones. *Contributions to Mineralogy and Petrology* **165**.

Bird, P. (2003). An updated digital model of plate boundaries. *Geochemistry, Geophysics, Geosystems* **4**. https://doi.org/10.1029/2001GC000252.

Brahm Scott, R. (2021) *Olivine-hosted MIs as recorders of processes and conditions of slab dehydration and magmatic differentiation in the subduction zones of northern Japan: a thesis presented in partial fulfilment of the requirements for the degree of Doctor of Philosophy in Earth Science at Massey University, Palmerston North*. New Zealand: Massey University.

Brahm, R., Zellmer, G. F., Kuritani, T., Sakamoto, N., Yurimoto, H., Nakagawa, M. & Sato, E. (2022). Olivine melt inclusion constraints on some intensive properties of subvolcanic crystal mushes and their evolution through boundary layer fractionation in northern Japan. *Journal of Petrology* **63**. https://doi.org/10.1093/petrology/egac016.

Cai, C., Wiens, D. A., Shen, W. & Eimer, M. (2018). Water input into the Mariana subduction zone estimated from ocean-bottom seismic data. *Nature* **563**, 389–392. https://doi.org/10.1038/s41586-018-0655-4.

Carroll, M. R. & Webster, J. D. (1994). Solubilities of sulfur, noble gases, nitrogen, chlorine, and fluorine in magmas. *Volatiles in Magmas* **30**, 231–280. https://doi.org/10.1515/9781501509674-013.

Churikova, T., Dorendorf, F. & Wörner, G. (2001). Sources and fluids in the mantle wedge below Kamchatka, evidence from across-arc geochemical variation. *Journal of Petrology* **42**, 1567–1593. https://doi.org/10.1093/petrology/42.8.1567.

Connolly, J. A. D. & Kerrick, D. M. (1987). An algorithm and computer program for calculating composition phase diagrams. *Calphad* **11**, 1–55. https://doi.org/10.1016/0364-5916(87)90018-6.

Connolly, J. A. D. & Petrini, K. (2002). An automated strategy for calculation of phase diagram sections and retrieval of rock properties as a function of physical conditions. *Journal of Metamorphic Geology* **20**, 697–708. https://doi.org/10.1046/j.1525-1314.2002.00398.x.

Corella Santa Cruz, C. R., Zellmer, G. F., Stirling, C. H., Straub, S. M., Brenna, M., Reid, M. R., Németh, K. & Barr, D. (2023). Transcrustal and source processes affecting the chemical characteristics of magmas in a hyperactive volcanic zone. *Geochimica et Cosmochimica Acta* **352**, 86–106. https://doi.org/10.1016/j.gca.2023.05.003.

Cruz-Uribe, A. M., Marschall, H. R., Gaetani, G. A. & Le Roux, V. (2018). Generation of alkaline magmas in subduction zones by partial melting of mélange diapirs—an experimental study. *Geology* **46**, 343–346. https://doi.org/10.1130/G39956.1.

Dalou, C., Koga, K. T., Shimizu, N., Boulon, J. & Devidal, J.-L. (2012). Experimental determination of F and cl partitioning between lherzolite and basaltic melt. *Contributions to Mineralogy and Petrology* **163**, 591–609. https://doi.org/10.1007/s00410-011-0688-2.

Danyushevsky, L. V., Della-Pasqua, F. N. & Sokolov, S. (2000). Re-equilibration of melt inclusions trapped by magnesian olivine phenocrysts from subduction-related magmas: petrological implications. *Contributions to Mineralogy and Petrology* **138**, 68–83. https://doi.org/10.1007/PL00007664.

Debret, B. & Sverjensky, D. (2017). Highly oxidising fluids generated during serpentinite breakdown in subduction zones. *Scientific Reports* **7**, 10351–10356. https://doi.org/10.1038/s41598-017-09626-y.

D'Mello, N. G., Zellmer, G. F., Kereszturi, G., Ubide, T., Procter, J. N. & Stewart, R. B. (2023). Crystal entrainment from cool, low-silica rocks into hot, high-silica melts: diverse primary melt compositions at Taranaki volcano, New Zealand. *Journal of the Geological Society* **180**. https://doi.org/10.1144/jgs2022-036.

Evans, K., Elburg, M. & Kamenetsky, V. (2012). Oxidation state of subarc mantle. *Geology* **40**, 783–786. https://doi.org/10.1130/G33037.1.

Faccenda, M., Burlini, L., Gerya, T. V. & Mainprice, D. (2008). Fault-induced seismic anisotropy by hydration in subducting oceanic plates. *Nature* **455**, 1097–1100. https://doi.org/10.1038/nature07376.

Feineman, M. D., Ryerson, F. J., DePaolo, D. J. & Plank, T. (2007). Zoisite-aqueous fluid trace element partitioning with implications for subduction zone fluid composition. *Chemical Geology* **239**, 250–265. https://doi.org/10.1016/j.chemgeo.2007.01.008.

Foley, S. F., Barth, M. G. & Jenner, G. A. (2000). Rutile/melt partition coefficients for trace elements and an assessment of the influence of rutile on the trace element characteristics of subduction zone magmas. *Geochimica et Cosmochimica Acta* **64**, 933–938. https://doi.org/10.1016/S0016-7037(99)00355-5.

Forneris, J. F. & Holloway, J. R. (2003). Phase equilibria in subducting basaltic crust: implications for H2O release from the slab. *Earth and Planetary Science Letters* **214**, 187–201. https://doi.org/10.1016/S0012-821X(03)00305-4.

Gaetani, G. A., Kent, A. J., Grove, T. L., Hutcheon, I. D. & Stolper, E. M. (2003). Mineral/melt partitioning of trace elements during hydrous peridotite partial melting. *Contributions to Mineralogy and Petrology* **145**, 391–405. https://doi.org/10.1007/s00410-003-0447-0.

Gavrilenko, M., Herzberg, C., Vidito, C., Carr, M. J., Tenner, T. & Ozerov, A. (2016). A calcium-in-olivine Geohygrometer and its application to subduction zone magmatism. *Journal of Petrology* **57**, 1811–1832. https://doi.org/10.1093/petrology/egw062.

Gill, J. B. (1981). Orogenic Andesites and plate tectonics. *Orogenic Andesites and Plate Tectonics*. https://doi.org/10.1007/978-3-642-68012-0.

Green, E. C. R., White, R. W., Diener, J. F. A., Powell, R., Holland, T. J. B. & Palin, R. M. (2016). Activity–composition relations for the calculation of partial melting equilibria in metabasic rocks. *Journal of Metamorphic Geology* **34**, 845–869. https://doi.org/10.1111/jmg.12211.

Grevemeyer, I., Ranero, C. R. & Ivandic, M. (2018). Structure of oceanic crust and serpentinization at subduction trenches. *Geosphere* **14**, 395–418. https://doi.org/10.1130/GES01537.1.

Grove, T. L., Chatterjee, N., Parman, S. W. & Médard, E. (2006). The influence of H2O on mantle wedge melting. *Earth and Planetary Science Letters* **249**, 74–89. https://doi.org/10.1016/j.epsl.2006.06.043.

Hacker, B. R. (2008). H2O subduction beyond arcs. *Geochemistry, Geophysics, Geosystems* **9**. https://doi.org/10.1029/2007GC001707.

Hayes, G. P., Moore, G. L., Portner, D. E., Hearne, M., Flamme, H., Furtney, M. & Smoczyk, G. M. (2018). Slab2, a comprehensive subduction zone geometry model. *Science* **362**, 58–61. https://doi.org/10.1126/science.aat4723.

Hermann, J. (2002). Allanite: thorium and light rare earth element carrier in subducted crust. *Chemical Geology* **192**, 289–306. https://doi.org/10.1016/S0009-2541(02)00222-X.

Hermann, J. & Green, D. H. (2001). Experimental constraints on high pressure melting in subducted crust. *Earth and Planetary Science Letters* **188**, 149–168. https://doi.org/10.1016/S0012-821X(01)00321-1.

Hermann, J. & Rubatto, D. (2009). Accessory phase control on the trace element signature of sediment melts in subduction zones. *Chemical Geology* **265**, 512–526. https://doi.org/10.1016/j.chemgeo.2009.05.018.

Hermann, J. & Spandler, C. J. (2008). Sediment melts at sub-arc depths: an experimental study. *Journal of Petrology* **49**, 717–740. https://doi.org/10.1093/petrology/egm073.

Herms, P., John, T., Bakker, R. J. & Schenk, V. (2012). Evidence for channelized external fluid flow and element transfer in subducting slabs (Raspas complex, Ecuador). *Chemical Geology* **310-311**, 79–96. https://doi.org/10.1016/j.chemgeo.2012.03.023.

Holland, T. & Blundy, J. (1994). Non-ideal interactions in calcic amphiboles and their bearing on amphibole-plagioclase thermometry. *Contributions to Mineralogy and Petrology* **116**, 433–447. https://doi.org/10.1007/BF00310910.

Ikeda, Y., Kagami, H., Katsui, Y. & Kurasawa, H. (1990). Variations in Nd and Sr isotope ratios of quaternary volcanic rocks from the southwestern Kurile arc: an implication for migration of fluid phases in the subduction zone. *Journal of Mineralogy, Petrology and Economic Geology* **85**, 1–9. https://doi.org/10.2465/ganko.85.1.

Ishimoto, H., Shuto, K. & Goto, Y. (2006). Middle Miocene to quaternary primary basalt and high magnesian andesite magmas of North Hokkaido, Japan: source mantle characteristics and degrees of partial melting. *Island Arc* **15**, 251–268. https://doi.org/10.1111/j.1440-1738.2006.00525.x.

Ishizuka, Y. (1999). Eruptive history of Rishiri volcano, northern Hokkaido, Japan. *Kazan* **44**, 23–40.

Ishizuka, Y. & Nakagawa, M. (1999). Petrological evolution of Rishiri volcano, northern Hokkaido, Japan. *Journal of Mineralogy Petrology and Economic Geology* **94**, 279–294. https://doi.org/10.2465/ganko.94.279.

Jacques, G., Hoernle, K., Gill, J., Hauff, F., Wehrmann, H., Garbe-Schönberg, D., van den Bogaard, P., Bindeman, I. & Lara, L. E. (2013). Across-arc geochemical variations in the southern volcanic zone, Chile (34.5-38.0°S): constraints on mantle wedge and slab input compositions. *Geochimica et Cosmochimica Acta* **123**, 218–243. https://doi.org/10.1016/j.gca.2013.05.016.

Jacques, G., Hoernle, K., Gill, J., Wehrmann, H., Bindeman, I. & Lara, L. E. (2014). Geochemical variations in the central southern volcanic zone, Chile (38-43°S): the role of fluids in generating arc magmas. *Chemical Geology* **371**, 27–45. https://doi.org/10.1016/j.chemgeo.2014.01.015.

Jégo, S. & Dasgupta, R. (2013). Fluid-present melting of sulfide-bearing ocean-crust: experimental constraints on the transport of sulfur from subducting slab to mantle wedge. *Geochimica et Cosmochimica Acta* **110**, 106–134. https://doi.org/10.1016/j.gca.2013.02.011.

Jégo, S. & Dasgupta, R. (2014). The fate of sulfur during fluid-present melting of subducting basaltic crust at variable oxygen fugacity. *Journal of Petrology* **55**, 1019–1050. https://doi.org/10.1093/petrology/egu016.

Jochum, K. P., Nohl, U., Herwig, K., Lammel, E., Stoll, B. & Hofmann, A. W. (2005). GeoReM: a new geochemical database for reference materials and isotopic standards. *Geostandards and Geoanalytical Research* **29**, 333–338. https://doi.org/10.1111/j.1751-908X.2005.tb00904.x.

John, T., Scherer, E. E., Haase, K. & Schenk, V. (2004). Trace element fractionation during fluid-induced eclogitization in a subducting slab: trace element and Lu–Hf–Sm–Nd isotope systematics. *Earth and Planetary Science Letters* **227**, 441–456. https://doi.org/10.1016/j.epsl.2004.09.009.

John, T., Scambelluri, M., Frische, M., Barnes, J. D. & Bach, W. (2011). Dehydration of subducting serpentinite: implications for halogen mobility in subduction zones and the deep halogen cycle. *Earth and Planetary Science Letters* **308**, 65–76. https://doi.org/10.1016/j.epsl.2011.05.038.

John, T., Gussone, N., Podladchikov, Y. Y., Bebout, G. E., Dohmen, R., Halama, R., Klemd, R., Magna, T. & Seitz, H.-M. (2012). Volcanic arcs fed by rapid pulsed fluid flow through subducting slabs. *Nature Geoscience* **5**, 489–492. https://doi.org/10.1038/ngeo1482.

Katsui, Y. (1953). Petro-chemical study on the lavas from volcano Rishiri, Hokkaido, Japan. *Journal of the Faculty of Science, Hokkaido University. Series 4, Geology and mineralogy* **8**, 245–258.

Katsui, Y. & Satoh, H. (1970). Geology of the Oshima-Oshima district. *Geological Survey of Japan* **16**.

Katsui, Y. & Yamamoto, M. (1981). The 1741-1742 activity of Oshima-Ōshima volcano, North Japan. *北海道大学理学部紀要 Journal of the Faculty of Science, Hokkaido University. Series 4, Geology and mineralogy* **19**, 527–536.

Katsui, Y., Ōba, Y., Ando, S., Nishimura, S., Masuda, Y., Kurasawa, H. & Fujimaki, H. (1978). Petrochemistry of the quaternary volcanic rocks of Hokkaido, North Japan. *北海道大学理学部紀要* **18**, 449–484.

Katsui, Y., Yamamoto, M., Nemoto, S. & Niida, K. (1979). Genesis of calc-alkalic andesites from Oshima-Ōshima and Ichinomegata volcanoes. *North Japan. 北海道大学理学部紀要* **19**, 157–168.

Kelley, K. A. & Cottrell, E. (2009). Water and the oxidation state of subduction zone magmas. *Science* **325**, 605–607. https://doi.org/10.1126/science.1174156.

Kelley, K. A., Plank, T., Grove, T. L., Stolper, E. M., Newman, S. & Hauri, E. (2006). Mantle melting as a function of water content beneath back-arc basins. *Journal of Geophysical Research: Solid Earth* **111**. https://doi.org/10.1029/2005JB003732.

Kelley, K. A., Plank, T., Newman, S., Stolper, E. M., Grove, T. L., Parman, S. & Hauri, E. H. (2010). Mantle melting as a function of water content beneath the Mariana arc. *Journal of Petrology* **51**, 1711–1738. https://doi.org/10.1093/petrology/egq036.

Kendrick, M. A., Arculus, R. J., Danyushevsky, L. V., Kamenetsky, V. S., Woodhead, J. D. & Honda, M. (2014). Subduction-related halogens (cl, Br and I) and H2O in magmatic glasses from Southwest Pacific Backarc basins. *Earth and Planetary Science Letters* **400**, 165–176. https://doi.org/10.1016/j.epsl.2014.05.021.

Kendrick, M. A., Hémond, C., Kamenetsky, V. S., Danyushevsky, L., Devey, C. W., Rodemann, T., Jackson, M. G. & Perfit, M. R. (2017). Seawater cycled throughout Earth's mantle in partially serpentinized lithosphere. *Nature Geoscience* **10**, 222–228. https://doi.org/10.1038/ngeo2902.

Kendrick, M. A., D'Andres, J., Holden, P. & Ireland, T. (2018). Halogens (F, cl, Br, I) in thirteen USGS, GSJ and NIST international rock and glass reference materials. *Geostandards and Geoanalytical Research* **42**, 499–511. https://doi.org/10.1111/ggr.12229.

Kendrick, M. A., Danyushevsky, L. V., Falloon, T. J., Woodhead, J. D., Arculus, R. J. & Ireland, T. (2020). SW Pacific arc and backarc lavas and the role of slab-bend serpentinites in the global halogen cycle. *Earth and Planetary Science Letters* **530**, 115921. https://doi.org/10.1016/j.epsl.2019.115921.

Kessel, R., Schmidt, M. W., Ulmer, P. & Pettke, T. (2005). Trace element signature of subduction-zone fluids, melts and supercritical liquids at 120–180 km depth. *Nature* **437**, 724–727. https://doi.org/10.1038/nature03971.

Kimura, G. (1996). Collision orogeny at arc-arc junctions in the Japanese Islands. *Island Arc* **5**, 262–275. https://doi.org/10.1111/j.1440-1738.1996.tb00031.x.

Kimura, J. I. (2017). Modeling chemical geodynamics of subduction zones using the arc basalt simulator version 5. *Geosphere* **13**, 992–1025. https://doi.org/10.1130/GES01468.1.

Kimura, J. I. & Nakajima, J. (2014). Behaviour of subducted water and its role in magma genesis in the NE Japan arc: a combined geophysical and geochemical approach. *Geochimica et Cosmochimica Acta* **143**, 165–188. https://doi.org/10.1016/j.gca.2014.04.019.

Kimura, J. I., Kent, A. J. R., Rowe, M. C., Katakuse, M., Nakano, F., Hacker, B. R., Van Keken, P. E., Kawabata, H. & Stern, R. J. (2010). Origin of cross-chain geochemical variation in quaternary lavas from the northern Izu arc: using a quantitative mass balance approach to identify mantle sources and mantle wedge processes. *Geochemistry, Geophysics, Geosystems* **11**. https://doi.org/10.1029/2010GC003050.

Kita, S., Nakajima, J., Hasegawa, A., Okada, T., Katsumata, K., Asano, Y. & Kimura, T. (2014). Detailed seismic attenuation structure beneath Hokkaido, northeastern Japan: arc-arc collision process, arc magmatism, and seismotectonics. *Journal of Geophysical Research: Solid Earth* **119**, 6486–6511. https://doi.org/10.1002/2014JB011099.

Klimm, K., Blundy, J. D. & Green, T. H. (2008). Trace element partitioning and accessory phase saturation during H2O-saturated melting of basalt with implications for subduction zone chemical fluxes. *Journal of Petrology* **49**, 523–553. https://doi.org/10.1093/petrology/egn001.

Kobayashi, T. (1987). Geology of Rishiri volcano. *Journal of Geological Society of Japan* **93**, 749–760_1. https://doi.org/10.5575/geosoc.93.749.

Konrad-Schmolke, M. & Halama, R. (2014). Combined thermodynamic–geochemical modeling in metamorphic geology: boron as tracer of fluid–rock interaction. *Lithos* **208-209**, 393–414. https://doi.org/10.1016/j.lithos.2014.09.021.

Krenn, E., Harlov, D. E., Finger, F. & Wunder, B. (2012). LREE-redistribution among fluorapatite, monazite, and allanite at high pressures and temperatures. *American Mineralogist* **97**, 1881–1890. https://doi.org/10.2138/am.2012.4005.

Kress, V. C. & Carmichael, I. S. E. (1991). The compressibility of silicate liquids containing Fe2O3 and the effect of composition, temperature, oxygen fugacity and pressure on their redox states.

Contributions to Mineralogy and Petrology **108**, 82–92. https://doi.org/10.1007/BF00307328.

Kuritani, T. (1998). Boundary layer crystallization in a basaltic magma chamber: evidence from Rishiri volcano, northern Japan. *Journal of Petrology* **39**, 1619–1640. https://doi.org/10.1093/petroj/39.9.1619.

Kuritani, T. (1999). Boundary layer fractionation constrained by differential information from the Kutsugata lava flow, Rishiri volcano, Japan. *Journal of Geophysical Research: Solid Earth* **104**, 29401–29417. https://doi.org/10.1029/1999JB900266.

Kuritani, T. (2001). Replenishment of a mafic magma in a zoned felsic magma chamber beneath Rishiri volcano, Japan. *Bulletin of Volcanology* **62**, 533–548. https://doi.org/10.1007/s004450000117.

Kuritani, T. & Nakamura, E. (2006). Elemental fractionation in lavas during post-eruptive degassing: evidence from trachytic lavas, Rishiri volcano, Japan. *Journal of Volcanology and Geothermal Research* **149**, 124–138. https://doi.org/10.1016/j.jvolgeores.2005.06.008.

Kuritani, T., Kitagawa, H. & Nakamura, E. (2005). Assimilation and fractional crystallization controlled by transport process of crustal melt: implications from an alkali basalt–dacite suite from Rishiri volcano, Japan. *Journal of Petrology* **46**, 1421–1442. https://doi.org/10.1093/petrology/egi021.

Kuritani, T., Yokoyama, T. & Nakamura, E. (2007). Rates of thermal and chemical evolution of magmas in a cooling magma chamber: a chronological and theoretical study on basaltic and andesitic lavas from Rishiri volcano, Japan. *Journal of Petrology* **48**, 1295–1319. https://doi.org/10.1093/petrology/egm018.

Kuritani, T., Yokoyama, T. & Nakamura, E. (2008). Generation of rear-arc magmas induced by influx of slab-derived supercritical liquids: implications from alkali basalt lavas from Rishiri volcano, Kurile arc. *Journal of Petrology* **49**, 1319–1342. https://doi.org/10.1093/petrology/egn027.

Kuritani, T., Yoshida, T., Kimura, J.-I., Takahashi, T., Hirahara, Y., Miyazaki, T., Senda, R., Chang, Q. & Ito, Y. (2014). Primary melt from Sannome-Gata volcano, NE Japan arc: constraints on generation conditions of rear-arc magmas. *Contributions to Mineralogy and Petrology* **167**. https://doi.org/10.1007/s00410-014-0969-7.

Kuritani, T., Kanai, C., Yamashita, S. & Nakagawa, M. (2019). Magma generation conditions at the Akita-Komagatake volcano, Northeast Japan arc: implications of across-arc variations in mantle melting parameters. *Lithos* **348-349**, 105197. https://doi.org/10.1016/j.lithos.2019.105197.

Kuritani, T., Sato, E., Wada, K., Matsumoto, A., Nakagawa, M., Zhao, D., Shimizu, K. & Ushikubo, T. (2021). Conditions of magma generation at the me-akan volcano, northern Japan. *Journal of Volcanology and Geothermal Research* **417**, 107323. https://doi.org/10.1016/j.jvolgeores.2021.107323.

Laske, G., Masters, G., Ma, Z. & Pasyanos, M. (2013). Update on CRUST1. 0-A 1-degree global model of Earth's CRUST. *Geophysical research abstracts: EGU General Assembly 2013, Vienna, Austria*, 2658.

Li, H. & Hermann, J. (2017). Chlorine and fluorine partitioning between apatite and sediment melt at 2.5 GPa, 800 C: a new experimentally derived thermodynamic model. *American Mineralogist* **102**, 580–594. https://doi.org/10.2138/am-2017-5891.

Li, H., Zhang, L., Bao, X., Wykes, J. L. & Liu, X. (2021). High sulfur solubility in subducted sediment melt under both reduced and oxidized conditions: with implications for S recycling in subduction zone settings. *Geochimica et Cosmochimica Acta* **304**, 305–326. https://doi.org/10.1016/j.gca.2021.04.001.

Manning, C. E. (2004). The chemistry of subduction-zone fluids. *Earth and Planetary Science Letters* **223**, 1–16. https://doi.org/10.1016/j.epsl.2004.04.030.

Marks, M. A. W., Kendrick, M. A., Eby, G. N., Zack, T. & Wenzel, T. (2017). The F, cl, Br and I contents of reference glasses BHVO-2G, BIR-1G, BCR-2G, GSD-1G, GSE-1G, NIST SRM 610 and NIST SRM 612. *Geostandards and Geoanalytical Research* **41**, 107–122. https://doi.org/10.1111/ggr.12128.

Marschall, H. R. & Schumacher, J. C. (2012). Arc magmas sourced from mélange diapirs in subduction zones. *Nature Geoscience* **5**, 862–867. https://doi.org/10.1038/ngeo1634.

Martin, A. K. (2011). Double saloon door tectonics in the Japan Sea, fossa Magna, and the Japanese Island arc. *Tectonophysics* **498**, 45–65. https://doi.org/10.1016/j.tecto.2010.11.016.

Martin, L. A. J., Wood, B. J., Turner, S. & Rushmer, T. (2011). Experimental measurements of trace element partitioning between Lawsonite, Zoisite and fluid and their implication for the composition of arc magmas. *Journal of Petrology* **52**, 1049–1075. https://doi.org/10.1093/petrology/egr018.

Martin, L., Hermann, J. R., Gauthiez-Putallaz, L., Whitney, D., Vitale Brovarone, A., Fornash, K. & Evans, N. J. (2014). Lawsonite geochemistry and stability–implication for trace element and water cycles in subduction zones. *Journal of Metamorphic Geology* **32**, 455–478. https://doi.org/10.1111/jmg.12093.

Martin, C., Flores, K. E. & Harlow, G. E. (2016). Boron isotopic discrimination for subduction-related serpentinites. *Geology* **44**, 899–902. https://doi.org/10.1130/G38102.1.

Martin, C., Flores, K. E., Vitale-Brovarone, A., Angiboust, S. & Harlow, G. E. (2020). Deep mantle serpentinization in subduction zones: insight from in situ B isotopes in slab and mantle wedge serpentinites. *Chemical Geology* **545**, 119637. https://doi.org/10.1016/j.chemgeo.2020.119637.

Moretti, R. & Baker, D. R. (2008). Modeling the interplay of fO2 and fS2 along the FeS-silicate melt equilibrium. *Chemical Geology* **256**, 286–298. https://doi.org/10.1016/j.chemgeo.2008.06.055.

Moriguti, T., Shibata, T. & Nakamura, E. (2004). Lithium, boron and lead isotope and trace element systematics of quaternary basaltic volcanic rocks in northeastern Japan: mineralogical controls on slab-derived fluid composition. *Chemical Geology* **212**, 81–100. https://doi.org/10.1016/j.chemgeo.2004.08.005.

Moyen, J. F. & Stevens, G. (2006). Experimental constraints on TTG Petrogenesis: implications for Archean geodynamics. *Archean Geodynamics and Environments* **164**, 149–175. https://doi.org/10.1029/164GM11.

Muth, M. J. & Wallace, P. J. (2021). Slab-derived sulfate generates oxidized basaltic magmas in the southern Cascade arc (California, USA). *Geology* **49**, 1177–1181. https://doi.org/10.1130/G48759.1.

Muth, M. J. & Wallace, P. J. (2022). Sulfur recycling in subduction zones and the oxygen fugacity of mafic arc magmas. *Earth and Planetary Science Letters* **599**, 117836. https://doi.org/10.1016/j.epsl.2022.117836.

Newman, S. & Lowenstern, J. B. (2002). VOLATILECALC: a silicate melt-H2O-CO2 solution model written in visual basic for excel. *Computers and Geosciences* **28**, 597–604. https://doi.org/10.1016/S0098-3004(01)00081-4.

Newton, R. C. & Manning, C. E. (2005). Solubility of anhydrite, $CaSO_4$, in NaCl–H_2O solutions at high pressures and temperatures: applications to fluid–rock interaction. *Journal of Petrology* **46**, 701–716. https://doi.org/10.1093/petrology/egh094.

Nielsen, S. G. & Marschall, H. R. (2017). Geochemical evidence for mélange melting in global arcs. *Science Advances* **3**, e1602402. https://doi.org/10.1126/sciadv.1602402.

Nikolaev, G. S., Ariskin, A., Barmina, G., Nazarov, M. & Almeev, R. (2016). Test of the Ballhaus–berry–Green Ol–Opx–Sp oxybarometer and calibration of a new equation for estimating the redox

state of melts saturated with olivine and spinel. *Geochemistry International* **54**, 301–320. https://doi.org/10.1134/S0016702916040078.

Northrup, C. J., Royden, L. H. & Burchfie, B. C. (1995). Motion of the Pacific plate relative to Eurasia and its potential relation to Cenozoic extension along the eastern margin of Eurasia. *Geology* **23**, 719–722. https://doi.org/10.1130/0091-7613(1995)023%3c0719:MOTPPR%3e2.3.CO;2.

Oppenheimer, C., Scaillet, B. & Martin, R. S. (2011). Sulfur degassing from volcanoes: source conditions, surveillance, plume chemistry and earth system impacts. *Reviews in Mineralogy and Geochemistry* **73**, 363–421. https://doi.org/10.2138/rmg.2011.73.13.

Pagé, L. & Hattori, K. (2017). Tracing halogen and B cycling in subduction zones based on obducted, subducted and forearc serpentinites of the Dominican Republic. *Scientific Reports* **7**, 17776. https://doi.org/10.1038/s41598-017-18139-7.

Pagé, L., Hattori, K., de Hoog, J. C. M. & Okay, A. I. (2016). Halogen (F, cl, Br, I) behaviour in subducting slabs: a study of lawsonite blueschists in western Turkey. *Earth and Planetary Science Letters* **442**, 133–142. https://doi.org/10.1016/j.epsl.2016.02.054.

Papale, P., Moretti, R. & Barbato, D. (2006). The compositional dependence of the saturation surface of H 2O + CO 2 fluids in silicate melts. *Chemical Geology* **229**, 78–95. https://doi.org/10.1016/j.chemgeo.2006.01.013.

Patino, L. C., Carr, M. J. & Feigenson, M. D. (1997). Cross-arc geochemical variations in volcanic fields in Honduras C.A.: progressive changes in source with distance from the volcanic front. *Contributions to Mineralogy and Petrology* **129**, 341–351. https://doi.org/10.1007/s004100050341.

Patino, L. C., Carr, M. J. & Feigenson, M. D. (2000). Local and regional variations in central American arc lavas controlled by variations in subducted sediment input. *Contributions to Mineralogy and Petrology* **138**, 265–283. https://doi.org/10.1007/s004100050562.

Patton, C., Hellstrom, J., Paul, B., Woodhead, J. H. & Hergt, J. (2011). Iolite: freeware for the visualization and processing of mass spectrometry data. *Journal of Analytical Atomic Spectrometry* **26**, 2508–2518. https://doi.org/10.1039/c1ja10172b.

Pearce, J. A. (1983). Role of the sub-continental lithosphere in magma genesis at active continental margins. *Continental Basalts and Mantle Xenoliths* , 230–249.

Pearce, J. A., Stern, R. J., Bloomer, S. H. & Fryer, P. (2005). Geochemical mapping of the Mariana arc-basin system: implications for the nature and distribution of subduction components. *Geochemistry, Geophysics, Geosystems* **6**. https://doi.org/10.1029/2004GC000895.

Peccerillo, A. & Taylor, S. R. (1976). Geochemistry of eocene calc-alkaline volcanic rocks from the Kastamonu area, northern Turkey. *Contributions to Mineralogy and Petrology* **58**, 63–81. https://doi.org/10.1007/BF00384745.

Perfit, M. R., Gust, D., Bence, A. E., Arculus, R. & Taylor, S. R. (1980). Chemical characteristics of island-arc basalts: implications for mantle sources. *Chemical Geology* **30**, 227–256. https://doi.org/10.1016/0009-2541(80)90107-2.

Plank, T. (2014) The Chemical Composition of Subducting Sediments. In: Holland H. D. & Turekian K. K. (eds) *Treatise on Geochemistry*, 2nd edn. Oxford: Elsevier, pp.607–629.

Plank, T. & Langmuir, C. H. (1998). The chemical composition of subducting sediment and its consequences for the crust and mantle. *Chemical Geology* **145**, 325–394. https://doi.org/10.1016/S0009-2541(97)00150-2.

Portnyagin, M., Hoernle, K., Plechov, P., Mironov, N. & Khubunaya, S. (2007). Constraints on mantle melting and composition and nature of slab components in volcanic arcs from volatiles (H_2O, S, cl, F) and trace elements in melt inclusions from the Kamchatka arc. *Earth and Planetary Science Letters* **255**, 53–69. https://doi.org/10.1016/j.epsl.2006.12.005.

Prouteau, G. & Scaillet, B. (2012). Experimental constraints on Sulphur behaviour in subduction zones: implications for TTG and adakite production and the global Sulphur cycle since the Archean. *Journal of Petrology* **54**, 183–213. https://doi.org/10.1093/petrology/egs067.

Putirka, K. D., Perfit, M., Ryerson, F. J. & Jackson, M. G. (2007). Ambient and excess mantle temperatures, olivine thermometry, and active vs. passive upwelling. *Chemical Geology* **241**, 177–206. https://doi.org/10.1016/j.chemgeo.2007.01.014.

Ranero, C. R., Phipps Morgan, J., McIntosh, K. & Reichert, C. (2003). Bending-related faulting and mantle serpentinization at the middle America trench. *Nature* **425**, 367–373. https://doi.org/10.1038/nature01961.

Rasmussen, D. J., Plank, T. A., Wallace, P. J., Newcombe, M. E. & Lowenstern, J. B. (2020). Vapor-bubble growth in olivine-hosted melt inclusions. *American Mineralogist* **105**, 1898–1919. https://doi.org/10.2138/am-2020-7377.

Rustioni, G., Audetat, A. & Keppler, H. (2021). The composition of subduction zone fluids and the origin of the trace element enrichment in arc magmas. *Contributions to Mineralogy and Petrology* **176**, 51. https://doi.org/10.1007/s00410-021-01810-8.

Sadofsky, S. J., Portnyagin, M., Hoernle, K. & van den Bogaard, P. (2008). Subduction cycling of volatiles and trace elements through the central American volcanic arc: evidence from melt inclusions Contrib. *Mineralogy and Petrology* **155**, 433–456. https://doi.org/10.1007/s00410-007-0251-3.

Scambelluri, M., Fiebig, J., Malaspina, N., Müntener, O. & Pettke, T. (2004). Serpentinite subduction: implications for fluid processes and trace-element recycling. *International Geology Review* **46**, 595–613. https://doi.org/10.2747/0020-6814.46.7.595.

Schmidt, M. W. & Poli, S. (1998). Experimentally based water budgets for dehydrating slabs and consequences for arc magma generation. *Earth and Planetary Science Letters* **163**, 361–379. https://doi.org/10.1016/S0012-821X(98)00142-3.

Schmidt, M. W., Vielzeuf, D. & Auzanneau, E. (2004). Melting and dissolution of subducting crust at high pressures: the key role of white mica. *Earth and Planetary Science Letters* **228**, 65–84. https://doi.org/10.1016/j.epsl.2004.09.020.

Shibata, T. & Nakamura, E. (1997). Across-arc variations of isotope and trace element compositions from quaternary basaltic volcanic rocks in northeastern Japan: implications for interaction between subducted oceanic slab and mantle wedge. *Journal of Geophysical Research* **102**, 8051–8064. https://doi.org/10.1029/96JB03661.

Shimaoka, A., Imamura, M. & Kaneoka, I. (2016). Beryllium isotopic systematics in island arc volcanic rocks from Northeast Japan: implications for the incorporation of oceanic sediments into island arc magmas. *Chemical Geology* **443**, 158–172. https://doi.org/10.1016/j.chemgeo.2016.08.032.

Shuto, K., Hirahara, Y., Ishimoto, H., Aoki, A., Jinbo, A. & Goto, Y. (2004). Sr and Nd isotopic compositions of the magma source beneath North Hokkaido, Japan: comparison with the back-arc side in the NE Japan arc. *Journal of Volcanology and Geothermal Research* **134**, 57–75. https://doi.org/10.1016/j.jvolgeores.2004.01.001.

Sorensen, S. S., Grossman, J. N. & Perfit, M. R. (1997). Phengite-hosted LILE enrichment in eclogite and related rocks: implications for fluid-mediated mass transfer in subduction zones and arc magma genesis. *Journal of Petrology* **38**, 3–34. https://doi.org/10.1093/petroj/38.1.3.

Spandler, C., Hermann, J., Arculus, R. & Mavrogenes, J. (2003). Redistribution of trace elements during prograde metamorphism from lawsonite blueschist to eclogite facies; implications for deep subduction-zone processes. *Contributions to Mineralogy and Petrology* **146**, 205–222. https://doi.org/10.1007/s00410-003-0495-5.

Spandler, C., Mavrogenes, J. & Hermann, J. (2007). Experimental constraints on element mobility from subducted sediments using high-P synthetic fluid/melt inclusions. *Chemical Geology* **239**, 228–249. https://doi.org/10.1016/j.chemgeo.2006.10.005.

Stolper, E. & Newman, S. (1994). The role of water in the petrogenesis of Mariana trough magmas. *Earth and Planetary Science Letters* **121**, 293–325. https://doi.org/10.1016/0012-821X(94)90074-4.

Straub, S. M. & Layne, G. D. (2003). The systematics of chlorine, fluorine, and water in Izu arc front volcanic rocks: implications for volatile recycling in subduction zones. *Geochimica et Cosmochimica Acta* **67**, 4179–4203. https://doi.org/10.1016/S0016-7037(03)00307-7.

Syracuse, E. M., van Keken, P. E., Abers, G. A., Suetsugu, D., Bina, C., Inoue, T., Wiens, D. & Jellinek, M. (2010). The global range of subduction zone thermal models. *Physics of the Earth and Planetary Interiors* **183**, 73–90. https://doi.org/10.1016/j.pepi.2010.02.004.

Tamura, Y., Tani, K., Chang, Q., Shukuno, H., Kawabata, H., Ishizuka, O. & Fiske, R. S. (2007). Wet and dry basalt magma evolution at Torishima volcano, Izu–Bonin arc, Japan: the possible role of phengite in the downgoing slab. *Journal of Petrology* **48**, 1999–2031. https://doi.org/10.1093/petrology/egm048.

Taniuchi, H., Kuritani, T., Yokoyama, T., Nakamura, E. & Nakagawa, M. (2020). A new concept for the genesis of felsic magma: the separation of slab-derived supercritical liquid. *Scientific Reports* **10**, 8698. https://doi.org/10.1038/s41598-020-65641-6.

Tatsumi, Y. (1986). Formation of the volcanic front in subduction zones. *Geophysical Research Letters* **13**, 717–720. https://doi.org/10.1029/GL013i008p00717.

Tatsumi, Y. (1989). Migration of fluid phases and genesis of basalt magmas in subduction zones. *Journal of Geophysical Research* **94**, 4697–4707. https://doi.org/10.1029/JB094iB04p04697.

Tatsumi, Y., Hamilton, D. L. & Nesbitt, R. W. (1986). Chemical characteristics of fluid phase released from a subducted lithosphere and origin of arc magmas: evidence from high-pressure experiments and natural rocks. *Journal of Volcanology and Geothermal Research* **29**, 293–309. https://doi.org/10.1016/0377-0273(86)90049-1.

Tollstrup, D., Gill, J., Kent, A., Prinkey, D., Williams, R., Tamura, Y. & Ishizuka, O. (2010). Across-arc geochemical trends in the Izu-Bonin arc: contributions from the subducting slab, revisited. *Geochemistry, Geophysics, Geosystems* **11**. https://doi.org/10.1029/2009GC002847.

Toplis, M. J. (2005). The thermodynamics of iron and magnesium partitioning between olivine and liquid: criteria for assessing and predicting equilibrium in natural and experimental systems. *Contributions to Mineralogy and Petrology* **149**, 22–39. https://doi.org/10.1007/s00410-004-0629-4.

Tovish, A., Schubert, G. & Luyendyk, B. P. (1978). Mantle flow pressure and the angle of subduction: non-Newtonian corner flows. *Journal of Geophysical Research: Solid Earth* **83**, 5892–5898. https://doi.org/10.1029/JB083iB12p05892.

Tsay, A., Zajacz, Z., Ulmer, P. & Sanchez-Valle, C. (2017). Mobility of major and trace elements in the eclogite-fluid system and element fluxes upon slab dehydration. *Geochimica et Cosmochimica Acta* **198**, 70–91. https://doi.org/10.1016/j.gca.2016.10.038.

Wade, J. A., Plank, T., Melson, W. G., Soto, G. J. & Hauri, E. H. (2006). The volatile content of magmas from Arenal volcano, Costa Rica. *Journal of Volcanology and Geothermal Research* **157**, 94–120. https://doi.org/10.1016/j.jvolgeores.2006.03.045.

Walker, J. A., Carr, M. J., Patino, L. C., Johnson, C. M., Feigenson, M. D. & Ward, R. L. (1995). Abrupt change in magma generation processes across the central American arc in southeastern Guatemala: flux-dominated melting near the base of the wedge to decompression melting near the top of the wedge. *Contributions to Mineralogy and Petrology* **120**, 378–390. https://doi.org/10.1007/BF00306515.

Wallace, P. J. (2005). Volatiles in subduction zone magmas: concentrations and fluxes based on melt inclusion and volcanic gas data. *Journal of Volcanology and Geothermal Research* **140**, 217–240. https://doi.org/10.1016/j.jvolgeores.2004.07.023.

Wallace, P. & Carmichael, I. S. E. (1992). Sulfur in basaltic magmas. *Geochimica et Cosmochimica Acta* **56**, 1863–1874. https://doi.org/10.1016/0016-7037(92)90316-B.

Walters, J., Cruz-Uribe, A. & Marschall, H. (2020). Sulfur loss from subducted altered oceanic crust and implications for mantle oxidation. *Geochemical Perspectives Letters* **13**, 36–41. https://doi.org/10.7185/geochemlet.2011.

Wehrmann, H., Hoernle, K., Garbe-Schönberg, D., Jacques, G., Mahlke, J. & Schumann, K. (2014). Insights from trace element geochemistry as to the roles of subduction zone geometry and subduction input on the chemistry of arc magmas. *International Journal of Earth Sciences* **103**, 1929–1944. https://doi.org/10.1007/s00531-013-0917-1.

Workman, R. K. & Hart, S. R. (2005). Major and trace element composition of the depleted MORB mantle (DMM). *Earth and Planetary Science Letters* **231**, 53–72. https://doi.org/10.1016/j.epsl.2004.12.005.

Yamada, C., Tsujimori, T., Chang, Q. & Kimura, J.-I. (2019). Boron isotope variations of Franciscan serpentinites, northern California. *Lithos* **334-335**, 180–189. https://doi.org/10.1016/j.lithos.2019.02.004.

Yamamoto, M. (1988). Picritic primary magma and its source mantle for Oshima-Ōshima and back-arc side volcanoes, Northeast Japan arc. *Contributions to Mineralogy and Petrology* **99**, 352–359. https://doi.org/10.1007/BF00375367.

Yoshida, T., Yamaguchi, T. & Kawasaki, Y. (1981). Internal structure of Kutsugata lava flow, Rishiri volcano. *The Journal of the Japanese Association of Mineralogists, Petrologists and Economic Geologists* **76**, 181–194. https://doi.org/10.2465/ganko1941.76.181.

Yoshida, T., Kimura, J. I., Yamada, R., Acocella, V., Sato, H., Zhao, D., Nakajima, J., Hasegawa, A., Okada, T., Honda, S., Ishikawa, M., Ardiansyah Prima, O. D., Kudo, T., Shibazaki, B., Tanaka, A. & Imaizumi, T. (2014). Evolution of late cenozoic magmatism and the crust-mantle structure in the NE japan arc. *Geological Society Special Publication* **385**, 335–387. https://doi.org/10.1144/SP385.15.